PL-TR-96-2015
Environmental Research Papers, No. 1185

A SIMPLE, CAUSAL METHOD TO INCORPORATE ANELASTIC ATTENUATION INTO FINITE-DIFFERENCE CALCULATIONS

Rong-Song Jih

21 December 1995

PHILLIPS LABORATORY
Directorate of Geophysics
AIR FORCE MATERIEL COMMAND
HANSCOM AFB, MA 01731-3010

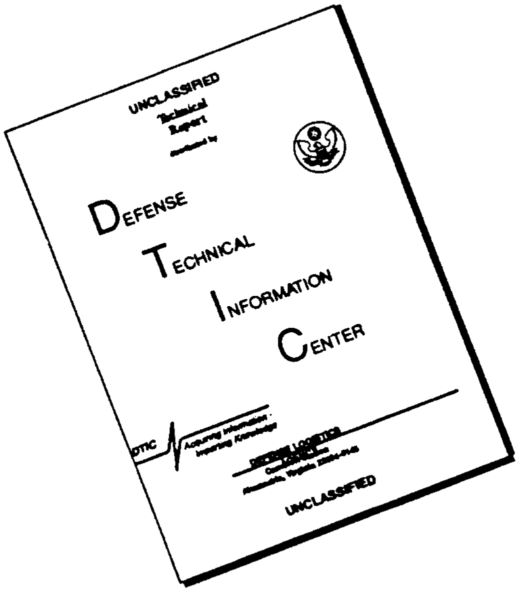
UNCLASSIFIED
Technical
Report
DEFENSE
TECHNICAL
INFORMATION
CENTER
DTIC
UNCLASSIFIED

"This technical report has been reviewed and is approved for publication."

JAMES F. LEWKOWICZ, Director
Earth Sciences Division

This report has been reviewed by the ESC Public Affairs Office (PA) and is releasable to the National Technical Information Service (NTIS).

Qualified requestors may obtain additional copies from the Defense Technical Information Center (DTIC). All others should apply to the National Technical Information Service (NTIS).

If your address has changed, or if you wish to be removed from the mailing list, or if the addressee is no longer employed by your organization, please notify PL/IM, 29 Randolph Road, Hanscom AFB, MA 01731-3010. This will assist us in maintaining current mailing list.

Do not return copies of this report unless contractual obligations or notices on a specific document requires that it be returned.

REPORT DOCUMENTATION PAGE

Form Approved
OMB No. 0704-0188

1. AGENCY USE ONLY *(Leave blank)*

2. REPORT DATE
21 December 1995

3. REPORT TYPE AND DATES COVERED
Scientific, Interim, 25 Oct - 24 Nov 1995

4. TITLE AND SUBTITLE
A Simple, Causal Method to Incorporate Anelastic Attenuation into Finite-Difference Calculations

5. FUNDING NUMBERS

PE 35999F	PE 621010
PR TERM	PR 7600
TA GM	TA 09
WU 88	WU 08

6. AUTHOR(S)
Rong-Song Jih*

7. PERFORMING ORGANIZATION NAME(S) AND ADDRESS(ES)
Phillips Laboratory (GPE)
29 Randolph Road
Hanscom AFB, MA 01731-3010

8. PERFORMING ORGANIZATION REPORT NUMBER
PL-TR-96-2015
ERP, No. 1185

9. SPONSORING/MONITORING AGENCY NAME(S) AND ADDRESS(ES)
HQ AFTAC/TTR
1030 South Highway 1A1
Patrick AFB, FL 32925-6001

10. SPONSORING/MONITORING AGENCY REPORT NUMBER

11. SUPPLEMENTARY NOTES
* Supported under AFTAC Project Authorization T/0121

12a. DISTRIBUTION/AVAILABILITY STATEMENT
Approved for Public Release; Distribution Unlimited

12b. DISTRIBUTION CODE

13. ABSTRACT *(Maximum 200 words)*

Current nuclear treaty monitoring interest has shifted to the verification of a comprehensive test ban treaty [CTBT], including the detection of the first test of potential proliferators. Predictive modeling capabilities are crucial, not just desirable, in the context of CTBT and proliferation monitoring. Synthetic seismograms generated with the linear-finite-difference [LFD] code are particularly useful for regions where earthquake or explosion data are not available. However, to date many LFD modeling exercises are still limited to the elastic case only. This report describes a simple approach to include anelastic attenuation in the LFD calculations. The algorithm gives a damping effect equivalent to what would be obtained by solving the viscoelastic wave equation. Testings of this algorithm with planar P, Rg, and L_g waves demonstrate that this method generates a frequency-independent damping over a rather broad band, which is equivalent to a Q increasing linearly with frequency. Any Q model that has a form other than $Q = Q_0 \cdot f^1$ can be simulated easily by superposing LFD results generated at several separate LFD runs corresponding to sampled $Q-f$ pairs of the desired Q structure. One shortcoming is that the performance of this attenuation operator degrades slightly at very low frequencies. Nevertheless, the shortcomings of this algorithm are outweighed by the simplicity. Most importantly, this procedure preserves the causality.

14. SUBJECT TERMS
Linear Finite-difference method, Anelastic attenuation, Visco-elastic equation, Damping, Quality factor, Lg, Rg

15. NUMBER OF PAGES
58

16. PRICE CODE

17. SECURITY CLASSIFICATION OF REPORT
Unclassified

18. SECURITY CLASSIFICATION OF THIS PAGE
Unclassified

19. SECURITY CLASSIFICATION OF ABSTRACT
Unclassified

20. LIMITATION OF ABSTRACT
SAR

CONTENTS

ILLUSTRATIONS

ACKNOWLEDGEMENTS

Conversations with Bob Blandford (AFTAC), Anton Dainty (PL), Dave Harkrider (BC), Keith McLaughlin (S-Cubed), and Howard Patton (LLNL) are gratefully acknowledged. The L_g eigenfunctions needed to synthesize the pure L_g wave packet are generated with Bob Herrmann's (SLU) software. The PSLIB *PostScript* library released by Paul Wessel (HIG) and Walter Smith (Scripps) has been used in generating most of the figures. This study was solely supported by Air Force Technical Applications Center. The views and conclusions contained in this manuscript are those of the author and should not be interpreted as representing the official polices, either expressed or implied, of the U.S. Air Force or the U.S. Government.

SUMMARY

Current nuclear treaty monitoring interest has shifted to the verification of a comprehensive test ban treaty [CTBT], including the detection of the first test of potential proliferators. Predictive modeling capabilities are crucial, not just desirable, in the context of CTBT and proliferation monitoring. Synthetic seismograms generated with the linear-finite-difference [LFD] code are particularly useful for regions where earthquake or explosion data are not available. However, to date many LFD modeling exercises are still limited to the elastic case only.

This report describes a simple approach to include anelastic attenuation linear-finite-difference calculations. The algorithm is extremely simple to implement, and it gives a damping effect equivalent to what would be obtained by solving the viscoelastic wave equation. Testings of this algorithm with planar P, R_g, and L_g waves demonstrate that this method generates a frequency-independent damping over a rather broad band, which is equivalent to a Q increasing linearly with frequency. Any Q model that has a form other than $Q = Q_0 \cdot f^1$ can be simulated easily by composing LFD results generated at several separate LFD runs corresponding to sampled $Q-f$ pairs of the desired Q structure. Like other techniques, this algorithm has its own limitations. One shortcoming is that the performance of this attenuation operator degrades slightly at the very low frequency. Nevertheless, the shortcomings of this algorithm are outweighed by the simplicity. Most importantly, this procedure preserves causality.

This algorithm has been applied to another research project under which a variety of mechanisms responsible for L_g blockage/weakening were examined and compared. With the help of this new algorithm, it is rather easy to equate the effects due to small-scale random heterogeneities (and other large-scale structural variations) with those due to the anelastic attenuation. The results are summarized in a companion report *"Waveguide effects of large-scale structural variation, anelastic attenuation, and random heterogeneity on SV Lg propagation: a finite-difference modeling study" (Report PL-TR-96-2016).*

Received for publication 21 December 1995.

A SIMPLE, CAUSAL METHOD TO INCORPORATE ANELASTIC ATTENUATION INTO FINITE-DIFFERENCE CALCULATIONS

1. INTRODUCTION

The incorporation of intrinsic attenuation due to an arbitrary absorption law is believed to be straightforward in frequency-domain methods. However, so far, many codes used in waveform synthesis (such as the reflectivity method and the wavenumber-integration method) can only handle a frequency-independent Q. Bache *et al.* (1981) found that L_g synthetics made for models with frequency-independent Q do not attenuate with the proper frequency dependence. If models are constructed that match L_g amplitude-distance relationship at 1 Hz, then L_g synthetics would attenuate too rapidly at higher frequencies.

For time-domain-based numerical methods, it has been very difficult to add the intrinsic attenuation because the anelastic stress-strain relation has the form of a convolution integral, which is intractable in a numerical computation. Vidale and Helmberger (1988) convolved finite-difference synthetics with a time-varying operator to model the effect of anelastic attenuation. This method is not suitable for media with spatially-varying Q. This method is also not appropriate when there are significant wave conversions (P to S *etc.*) in media where Q_P is not equal to Q_S. The first successful attempt to incorporate realistic attenuation laws into time-domain methods was made by Day and Minster (1984) (see also Minster *et al.*, 1991) based on the method of Pade approximation, which yields an expansion of the frequency-dependent viscoelastic modulus into a rational function. Emmerich and Korn (1987) propose a slightly different method based on the rheological model of the generalized Maxwell body, which has a modulus of the desired rational form. The major inconvenience of these approaches is that they demand a continual storage of five or more time steps of the wave field, depending on the accuracy of the approximation. The non-causal nature of some of these techniques is another fundamental drawback, at least conceptually, since in reality the anelastic attenuation of the Earth should act in a causal manner. That is, the dissipation of energy should occur as soon as the seismic wave arrives, and the resulting displacement at the current time step should not be dependent on that of the future.

With all these considerations in mind, a different procedure is developed in this study to incorporate the anelastic attenuation. It turns out that if we drop the ambitious attempt of imposing an arbitrary (that is, user-defined) frequency dependence on the Q operator, then it becomes very easy to implement a causal, phase-independent damping operator which is quite suitable for the linear finite-difference (LFD) calculation. Several researchers have demonstrated that the performance of commonly used absorbing boundary conditions can be greatly improved if a viscous damping zone is added to the grid boundary (Cerjan *et al.*, 1985; Levander, 1985a). The damping zone simply reduces the amplitude in a pointwise manner. There is no reason why this technique cannot be exploited to model the anelastic attenuation.

The LFD method has the advantage that the solution contains all conversions and all orders of multiple scattering. It permits examinations of fairly general models with arbitrary complex variations in material properties and free-surface geometry. Furthermore, it does not require many assumptions commonly invoked in other theoretical approaches. The basic limitations to the LFD method are the computational cost and memory requirements. These constrain the size of the grid and the number of time steps that can be calculated in a reasonable time. Despite the limitations, LFD is still one of the most powerful and popular modeling tools in generating realistic synthetic seismograms, and it is extremely desirable to have a convenient means to incorporate anelastic attenuation into LFD calculations. In this report, a causal procedure for this purpose is derived and discussed, followed by three sets of LFD experiments. Different seismic waves are used as the initial pulse in these examples to demonstrate the effectiveness of this algorithm.

2. METHOD

Consider the simplest isotropic homogeneous medium in which the amplitude of seismic waves decays exponentially with travel distance:

$$A(f, \Delta) = A_0(f) \cdot G = A_0(f) \cdot e^{-\gamma \cdot \Delta} \ , \qquad [1]$$

where $\gamma = \frac{\pi \cdot f}{U \cdot Q}$, U is the group velocity, and Δ is the distance traveled. In LFD calculations, Δ is taken to be the distance that the seismic wave would travel within one temporal step of the LFD iteration, that is, $\Delta = U \cdot dt$. Thus G can also be written as $e^{-\frac{\pi \cdot f \cdot dt}{Q}}$. There exists a constant η such that

$$G = e^{-\gamma \cdot \Delta} = 1 - \eta \cdot \gamma \cdot \Delta \ . \qquad [2]$$

It implies that $G = 1 - \frac{\eta \cdot \pi \cdot dt \cdot f}{Q}$ and hence $Q = Q_0 \cdot f$ if we define Q_0 to be $\frac{\eta \cdot dt \cdot \pi}{1 - G}$. If the damping term G is a function of the grid coordinate only and invariant with frequency, then we would have a Q increasing linearly with frequency. If, however, a frequency-dependent G is used in separate LFD simulations, then combining the band-limited LFD results would produce the solution for that particular frequency-dependent Q model. Here the parameter η is a function of γ or G, and the means of determining η will be discussed later. In practice, however, the users only need to specify a multiplicative constant G slightly less than 1 for each grid point. These localized damping factors are used to modify the displacement field pointwise at each iteration step. The decay rate (γ) and the quality factor (Q) can be determined later after the finite-difference calculation is done. A possible drawback of this approach is that if a specific frequency-dependent Q model is desired, then several separate LFD simulations need to be carried out for each frequency–Q pair of interest, as discussed above. Nevertheless, this possible shortcoming of this approach is outweighed by its simplicity. More importantly, this procedure preserves the causality. Another characteristic of this approach is that, given a damping factor G in a P-SV LFD calculation, $Q_0 = \frac{\eta \cdot dt \cdot \pi}{1 - G}$ would be applicable to both P and S phases. Thus Q_P and Q_S should be about the same.

So far we have derived several necessary conditions for an anelastic attenuation model, based on the desired exponential decay of seismic amplitude. In the following, we shall take a schematic view of this proposed algorithm. Consider the heterogeneous acoustic wave equation in the nondissipative medium:

$$\frac{\partial^2 P}{\partial t^2} = c^2(x, z)\left[\frac{\partial^2 P}{\partial x^2} + \frac{\partial^2 P}{\partial z^2}\right] \ , \qquad [3]$$

where P is the acoustic displacement potential, and c(x, z) is the acoustic velocity at the node (x, z).

LFD iteratively solves for the current pressure at (x, z) using the past pressure within a spatially-limited region surrounding the grid (x, z). The actual size of the temporal and spatial buffers required depends on the order of the LFD scheme. At each time step, the resulting unattenuated pressure P is then multiplied by the damping G to get the dissipated $\tilde{P}$. Once the whole pressure field is updated and dissipated (grid by grid) with the corresponding spatial damping factors, the standard LFD iteration restarts for the next pressure field without damping, and then damping factors are applied again. The procedure for the P-SV LFD calculation is exactly the same. It should be obvious that the extra calculation and memory required in this procedure are minimum. We can envision the pointwise damping factor as a degenerate digital filter which has only one point of temporal span (that is, memory). It can be regarded as the limiting case of the convolutional integral of many attenuation operators typically used in the frequency-domain approach.

The attenuated pressure, $\tilde{P} = P \cdot G$, can also be written as

$$\tilde{P} = P - \frac{\eta \cdot \pi \cdot dt \cdot f}{Q} \cdot P \,. \qquad [4]$$

That is, $\tilde{P}$ can be obtained by adjusting the undissipated P a little. The coefficient of pressure loss, $\frac{\eta \cdot \pi \cdot dt \cdot f}{Q}$ is very similar to the coefficient of the friction term which Levander (1985a) (and Frankel and Wennerberg, 1987) used in the telegraphy equation. The difference is that we have added the η term here to obtain the correct relationship between *Q* and the damping effect.

3. EXAMPLE 1: P-WAVE EXPERIMENT

The first example includes four separate LFD runs to test the propagation of a normally incident P wave through one elastic and three anelastic models. The whole space has compressional and shear velocities of 6.20 and 3.58 km/sec, respectively. The LFD grid has 500 nodes in the Z direction, and an absorbing boundary condition is applied to the top of the grid. The spatial and temporal spacings are 250 meters and 25 ms, respectively. In each test, the initial incident wave is a planar pulse with a shape of the derivative of Gaussian curve. The pulse is 32 grids long and centered at 1.5 Hz. For the three anelastic models, the damping factors are arbitrarily set to (A) 0.995, (B) 0.999, and (C) 0.9995, respectively. Figure 1 shows the vertical-component record sections of both the elastic model (top) and the anelastic model A with a damping factor of 0.995 (bottom), plotted in the same scale. In this example (and other examples given in latter sections), the geometrical spreading is not present in the LFD solution, and hence the standard one-station spectral analysis can be used to measure the amplitude decay and *Q* without the need to correct for the geometrical spreading first. A signal window of 25.6 seconds (1024 points) is used to compute the spectral ratio and the quality factor (Figures 2 and 3 show examples). The elastic model gives a γ less than 0.0001, which can be regarded as a measure of the numerical accuracy of the 2nd-order explicit LFD scheme used here. Higher-order LFD schemes should yield a γ even smaller for the elastic case. Figure 4 shows the spectral ratio of trace No. 1 to trace No. 16 of the model A. These two sensors are 75 km apart. It is interesting to note that actually the spectral ratio (and hence the resulting γ) is nearly a constant over a rather broad band. The γ of this model, measured at a suite of sensors evenly spread over a wide range, is consistently 0.018. The γ values of models B and C are 0.003 and 0.002, respectively. Table 1 below lists the γ and quality factors measured at fourteen sensors. In each case, the resulting *Q* is clearly a linear function of frequency.

Futterman (1962) showed that if a linear theory of wave propagation is assumed, then the presence of absorption is a necessary and sufficient condition for the presence of dispersion. He gave an excellent discussion of absorption-dispersion pairs. Using the condition of causality, he derived a Kramers-Kronig relation that allows one to calculate the dispersion for a given absorption function. (See also Ganley 1981; Liu *et al.*, 1976; Jacobson, 1987.) For frequency-independent *Q* models, this often leads to a noticeable broadening in the signal pulse as the seismic pulse travels to longer distances. In the special case of frequency-independent damping (γ), or equivalently, $Q = Q_0 \cdot f$ (such as the damping we used here), there should be no significant broadening. The dispersion is present, as a combined result of the causality and the grid dispersion. This is illustrated in Figure 1.

Table 1. P-wave Experiment with Three Anelastic Models

Model	Sensor	1 Hz		1.5 Hz		2 Hz		2.5 Hz	
ID, G	Range (km)	Q_0	γ	Q	γ	Q	γ	Q	γ
A, 0.995	75	28	0.018	42	0.018	59	0.017	75	0.017
A, 0.995	70	28	0.018	42	0.018	59	0.017	75	0.017
A, 0.995	65	28	0.018	42	0.018	59	0.017	75	0.017
A, 0.995	60	28	0.018	42	0.018	59	0.017	75	0.017
A, 0.995	55	28	0.018	42	0.018	59	0.017	75	0.017
A, 0.995	50	28	0.018	42	0.018	59	0.017	75	0.017
A, 0.995	45	28	0.018	42	0.018	59	0.017	75	0.017
A, 0.995	40	28	0.018	42	0.018	59	0.017	75	0.017
A, 0.995	35	28	0.018	42	0.018	59	0.017	75	0.017
A, 0.995	30	28	0.018	42	0.018	59	0.017	75	0.017
A, 0.995	25	28	0.018	42	0.018	59	0.017	75	0.017
A, 0.995	20	28	0.018	42	0.018	59	0.017	75	0.017
A, 0.995	15	28	0.018	42	0.018	59	0.017	75	0.017
A, 0.995	10	28	0.018	42	0.018	59	0.017	75	0.017
B, 0.999	75	156	0.003	228	0.003	303	0.003	369	0.003
B, 0.999	70	155	0.003	228	0.003	304	0.003	388	0.003
B, 0.999	65	154	0.003	229	0.003	305	0.003	387	0.003
B, 0.999	60	154	0.003	229	0.003	306	0.003	378	0.003
B, 0.999	55	154	0.003	229	0.003	307	0.003	380	0.003
B, 0.999	50	154	0.003	229	0.003	308	0.003	386	0.003
B, 0.999	45	154	0.003	229	0.003	308	0.003	384	0.003
B, 0.999	40	154	0.003	229	0.003	308	0.003	379	0.003
B, 0.999	35	154	0.003	229	0.003	308	0.003	381	0.003
B, 0.999	30	154	0.003	229	0.003	307	0.003	390	0.003
B, 0.999	25	154	0.003	229	0.003	306	0.003	383	0.003
B, 0.999	20	154	0.003	228	0.003	304	0.003	375	0.003
B, 0.999	15	153	0.003	225	0.003	303	0.003	383	0.003
B, 0.999	10	154	0.003	228	0.003	305	0.003	380	0.003
C, 0.9995	75	323	0.002	466	0.002	608	0.002	708	0.002
C, 0.9995	70	318	0.002	464	0.002	609	0.002	787	0.002
C, 0.9995	65	316	0.002	464	0.002	610	0.002	792	0.002
C, 0.9995	60	317	0.002	465	0.002	613	0.002	755	0.002
C, 0.9995	55	317	0.002	463	0.002	616	0.002	753	0.002
C, 0.9995	50	318	0.002	464	0.002	620	0.002	778	0.002
C, 0.9995	45	316	0.002	464	0.002	625	0.002	786	0.002
C, 0.9995	40	315	0.002	460	0.002	626	0.002	760	0.002
C, 0.9995	35	317	0.002	462	0.002	631	0.002	751	0.002
C, 0.9995	30	314	0.002	460	0.002	629	0.002	799	0.002
C, 0.9995	25	317	0.002	467	0.002	629	0.002	801	0.002
C, 0.9995	20	313	0.002	459	0.002	615	0.002	745	0.002
C, 0.9995	15	303	0.002	442	0.002	601	0.002	772	0.002
C, 0.9995	10	313	0.002	457	0.002	613	0.002	764	0.002

It was shown in the previous section that $Q_0 = \frac{\eta \cdot dt \cdot \pi}{1 - G}$, given a damping factor G in a P-SV LFD calculation. Since this Q_0 formula is applicable to both P and S phases, Q_P and Q_S should be about the same. This can easily be tested by using identical grid parameters in the LFD experiments but with different initial pulse types, as shown in Table 2 below.

Table 2. S-wave Experiment with Three Anelastic Models

Model	Sensor	1 Hz		1.5 Hz		2 Hz		2.5 Hz	
ID, G	Range (km)	Q_0	γ	Q	γ	Q	γ	Q	γ
A, 0.995	200	27	0.033	40	0.033	56	0.031	75	0.029
A, 0.995	160	27	0.033	40	0.033	56	0.031	71	0.031
A, 0.995	120	26	0.034	40	0.033	57	0.031	70	0.031
A, 0.995	80	26	0.034	40	0.033	57	0.031	71	0.031
A, 0.995	40	26	0.035	40	0.033	57	0.031	71	0.031
B, 0.999	200	146	0.006	223	0.006	299	0.006	362	0.006
B, 0.999	160	146	0.006	223	0.006	297	0.006	363	0.006
B, 0.999	120	146	0.006	223	0.006	297	0.006	363	0.006
B, 0.999	80	146	0.006	223	0.006	297	0.006	363	0.006
B, 0.999	40	145	0.006	223	0.006	297	0.006	362	0.006
C, 0.9995	200	303	0.003	453	0.003	611	0.003	734	0.003
C, 0.9995	160	304	0.003	451	0.003	598	0.003	726	0.003
C, 0.9995	120	304	0.003	451	0.003	598	0.003	726	0.003
C, 0.9995	80	305	0.003	451	0.003	598	0.003	727	0.003
C, 0.9995	40	304	0.003	451	0.003	598	0.003	727	0.003

Based on the results in Tables 1 and 2, we can solve for η in each case (Table 3). It should be emphasized (again) however, that the parameter η is introduced merely for convenience in deriving the algorithm. In practice, it is not necessary to determine the value of η in advance to incorporate the damping effect into the LFD calculation.

Table 3. Damping Factor and Associated Q_0 and η

Damping	P-wave Result		S-wave Result	
G	Q_0(P)	η	Q_0(S)	η
0.9950	28	$5.6/\pi$	27	$5.4/\pi$
0.9990	154	$6.1/\pi$	146	$5.8/\pi$
0.9995	317	$6.3/\pi$	303	$6.1/\pi$

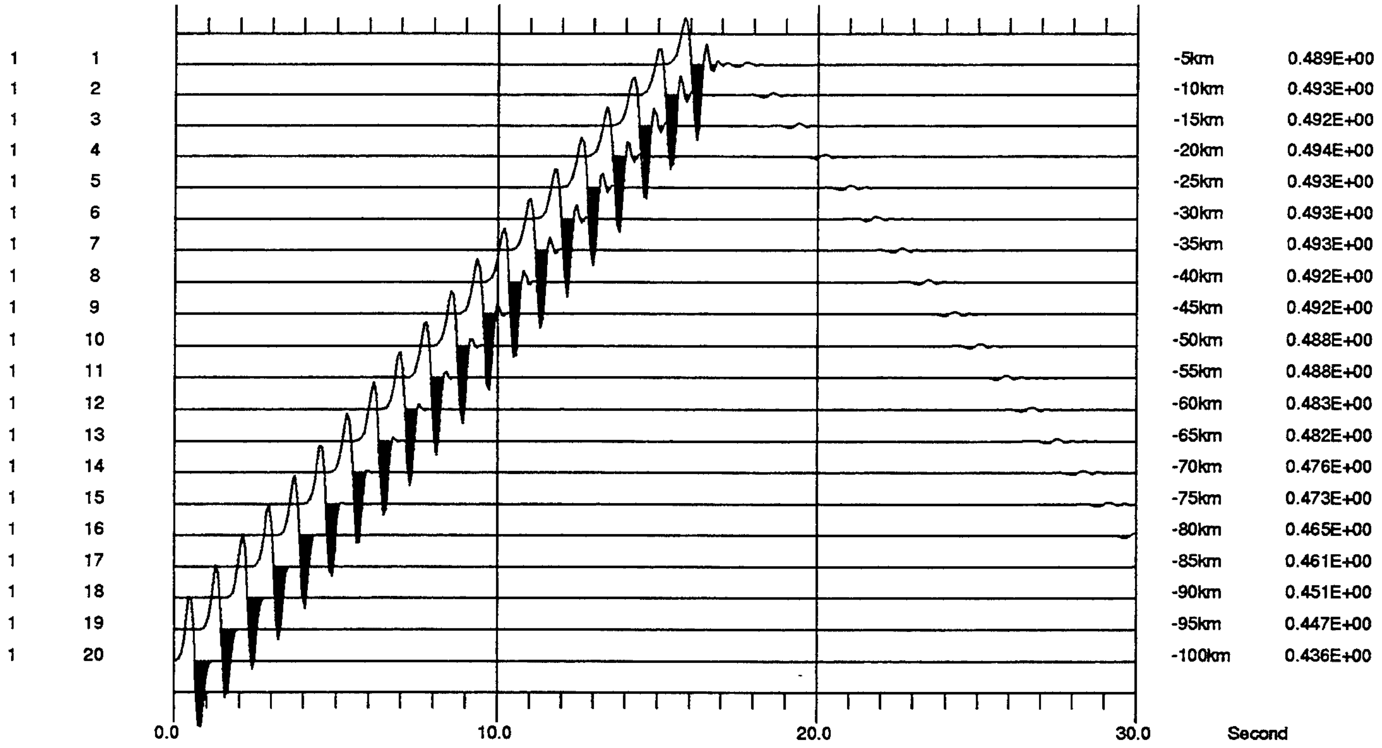

P wave, model no_Q, dx=dz=250m, dt=25ms

VERT, same scale, decimated by 3

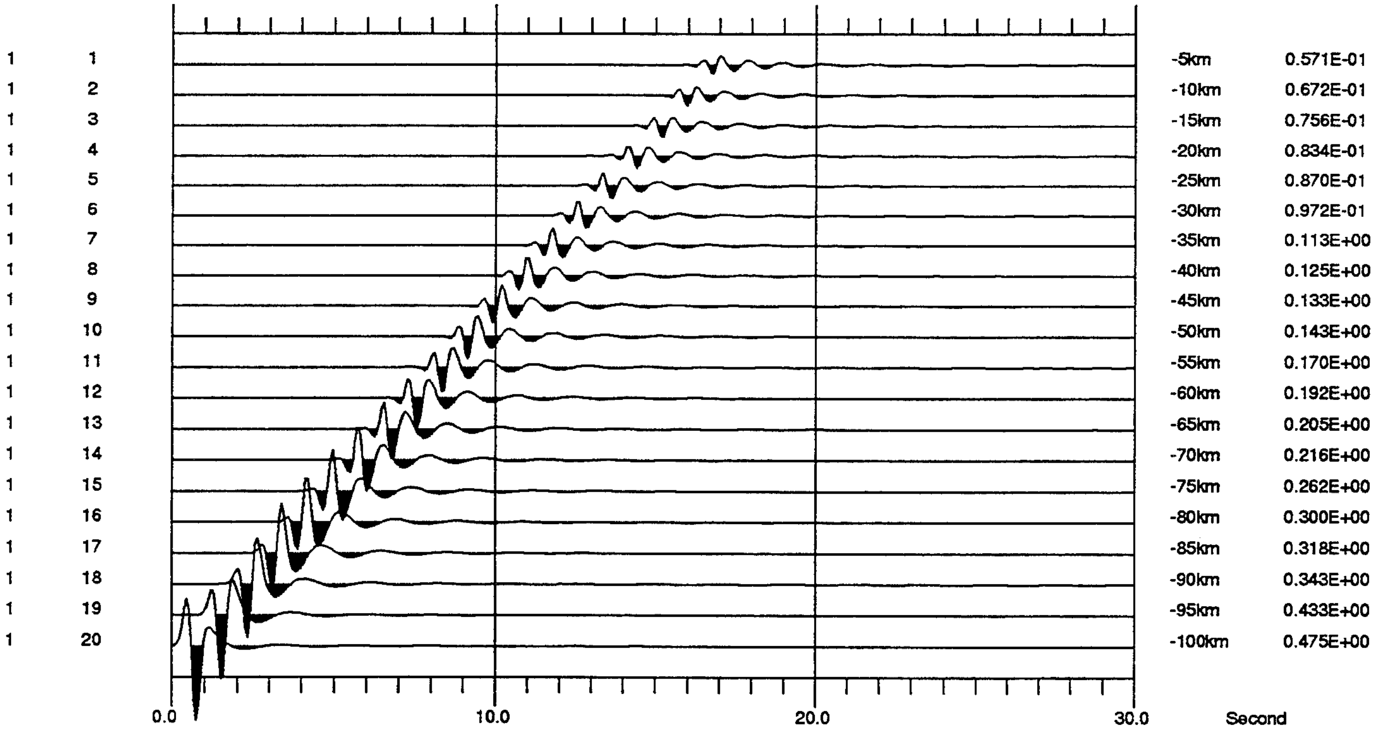

P wave, model Q.995, dx=dz=250m, dt=25ms

VERT, same scale, decimated by 3

Figure 1. Vertical-component record sections of normally-incident planar P waves in the elastic (top) and anelastic (bottom) whole-space models, respectively. Sensors are 5 km apart.

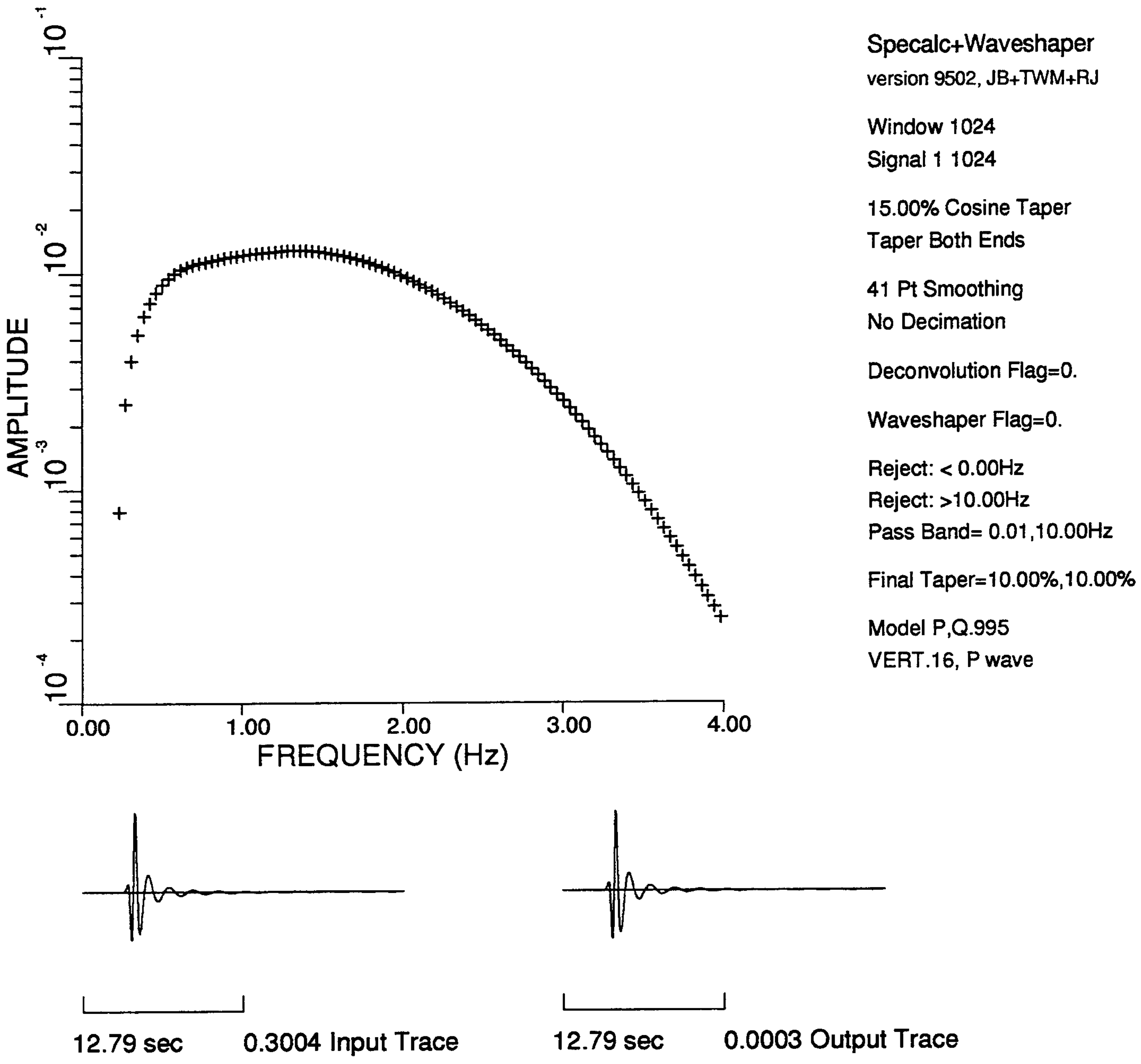

Specalc+Waveshaper
version 9502, JB+TWM+RJ

Window 1024
Signal 1 1024

15.00% Cosine Taper
Taper Both Ends

41 Pt Smoothing
No Decimation

Deconvolution Flag=0.

Waveshaper Flag=0.

Reject: < 0.00Hz
Reject: >10.00Hz
Pass Band= 0.01,10.00Hz

Final Taper=10.00%,10.00%

Model P,Q.995
VERT.16, P wave

Figure 2. Amplitude spectrum of the vertical-component LFD synthetic displacement seismogram recorded at sensor No. 16 of the anelastic model (A) which has a damping factor of 0.995.

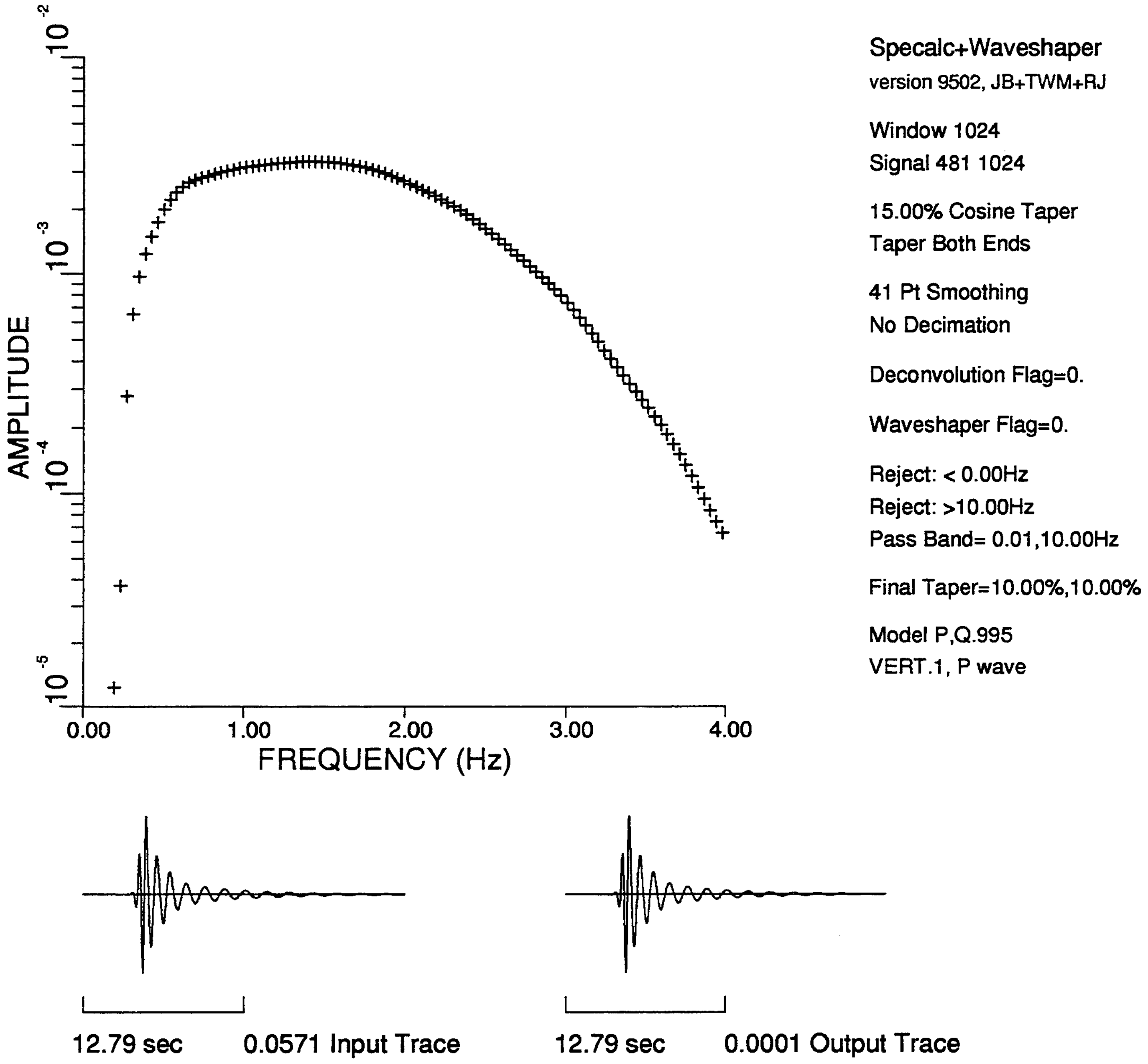

Specalc+Waveshaper
version 9502, JB+TWM+RJ

Window 1024
Signal 481 1024

15.00% Cosine Taper
Taper Both Ends

41 Pt Smoothing
No Decimation

Deconvolution Flag=0.

Waveshaper Flag=0.

Reject: < 0.00Hz
Reject: >10.00Hz
Pass Band= 0.01,10.00Hz

Final Taper=10.00%,10.00%

Model P,Q.995
VERT.1, P wave

Figure 3. Same as Figure 2 except for sensor No. 1, which is 75 km beyond sensor No. 16.

TGAL RATIO vers 1.5 (JB+TWM+RAW+RJ)

Thu Nov 9 08:07:24 1995

Model P,Q.995, ratio: No.1 / No.16, 75 km apart

NOISE POWER NOT SUBTRACTED FROM SIGNAL POWER

S/N POWER THRESHOLD = 2.0

NO SMOOTHING

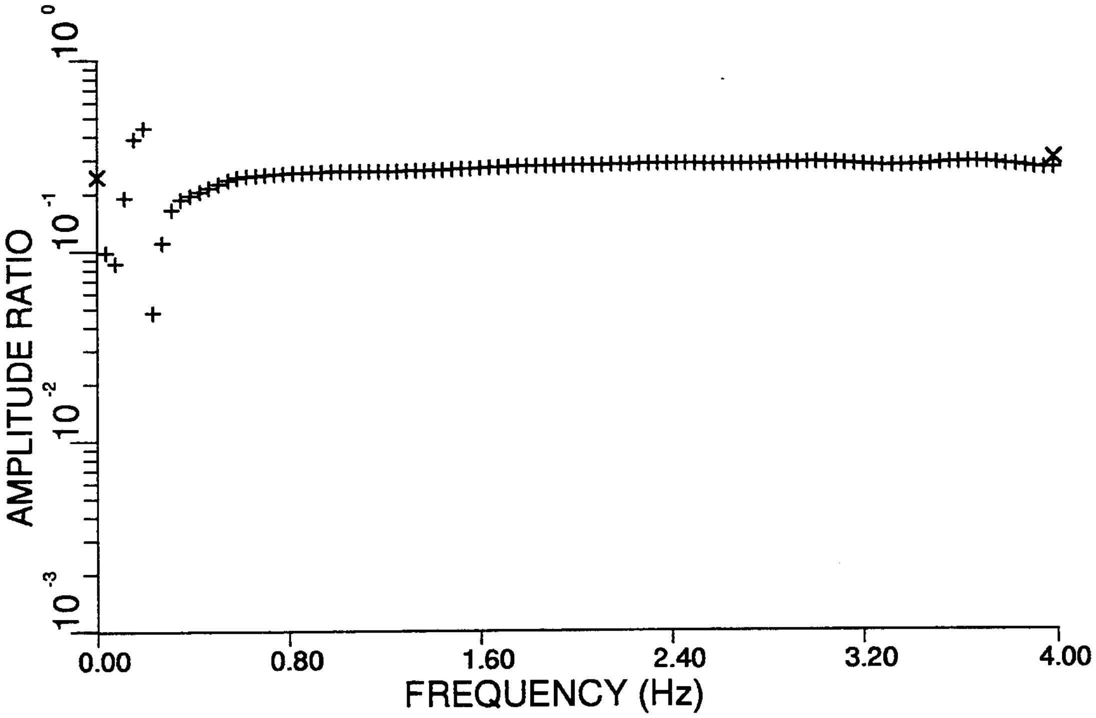

FREQ BAND	SLOPE	+/-	Y INTERC	AV INTEG	AV RATIO	SD
0.75-1.25	2.175e-02	1.993e-03	2.441e-01	-5.906e-01	-5.903e-01	3.498e-03
1.75-2.25	1.622e-02	1.483e-03	2.563e-01	-5.588e-01	-5.589e-01	2.599e-03
1.00-2.00	3.685e-02	1.608e-03	2.341e-01	-5.754e-01	-5.752e-01	1.128e-02
2.00-3.00	7.322e-03	2.015e-03	2.682e-01	-5.532e-01	-5.532e-01	3.577e-03
0.80-2.40	3.114e-02	8.365e-04	2.387e-01	-5.723e-01	-5.723e-01	1.479e-02

Figure 4. Spectral amplitude ratio (shown in log scale) of synthetic seismograms No. 1 to No. 16 (*cf.* Figures 2 and 3) of the anelastic model (A) which has a damping factor of 0.995. The amplitude ratio is nearly a constant over a rather broad band, which corresponds to a Q increasing linearly with frequency (see Table 1).

4. EXAMPLE 2: Lg-WAVE EXPERIMENT

In the second example we test the applicability of the proposed method to L_g waves with a single-layer crustal model. The pure L_g wave packet is injected into a stratified portion of the LFD grid as the reference initial condition to trigger all LFD calculations. An obvious advantage of this approach is that the effect due to different types of heterogeneity on L_g phase can be easily isolated and evaluated. The algorithm generating the incident L_g wave packet can be found in Jih (1995) and it is analogous to the one Boore (1970) developed for the fundamental-mode Love wave packet. The same approach has also been extensively used in elastic (P-SV) LFD simulations of R_g propagation/scattering problems. Among many others using the approach are: Levander (1985b), Toksoz et al. (1986), McLaughlin and Jih (1986, 1987), and Jih (1993b, 1996).

On real seismograms, the L_g phase often lacks a clear onset, but it does have a well-defined amplitude maximum with a group velocity around 3.5 km/sec. The L_g waves are basically the interference of multiply reflected S waves bouncing back and forth between the free surface and the Moho. We can envision that a system of planar S waves is set off at the Moho at equal delay with the same post-critical inclination, while another system of planar S waves is set off at the free surface in a symmetric manner, which corresponds to the bundle of reflected waves. If these two systems of waves (or rays) are properly confined in the same stratified region of the crust, they will establish repetitive reflections (at both the free surface and the Moho) with constructive interferences. By adjusting the time delay between the consecutive S wavefronts, we can obtain a denser (or coarser) interference pattern. The L_g waves can also be described as the superposition of many higher-mode surface waves that interfere to give the complex observed waveforms. These modes correspond to waves trapped in the crustal wave guide.

The pure L_g wave packet generated with the procedure described in Jih (1995, 1996) exhibits all these expected features. Figure 5 gives the vertical-component snapshots of L_g wave propagation in an anelastic single-layer crustal model taken at a temporal spacing of 10 seconds. The homogeneous crust is 30 km thick with $P-$ and $S-$wave velocities of 6.2 and 3.58 km/sec, respectively. The damping factor in the crust is set to 0.999. Since no scattering mechanism is present, the checkerboard-like pattern due to the constructive interference of repeatedly reflected S waves trapped in the crust is retained at all times (Figure 5). This chessboard-like pattern undoubtedly indicates that the two commonly quoted interpretations of L_g waves, either as multiply reflected S waves or as higher-mode surface waves, are indeed adequate. Note that the computational grid was shifted at 15 seconds (not shown) to stretch the lateral span of the grid. The "marching grid" technique is described in Jih (1993a).

Figure 6 displays the record section of the vertical-component synthetics of this anelastic model.

For comparison, the record section corresponding to the elastic case is also included. We find that several parameters, including the group velocity and the attenuation, can be more reliably measured with synthetics recorded at greater depths. Figure 7 shows the record sections at a depth of 10 km. Based on these seismic sections, the group velocity of L_g wave packet is determined to be 3.33 km/sec, which is appropriate for areas like the western U.S.

Table 4 lists the quality factors and amplitude ratios measured at a suite of sensors spread from 130 to 180 km at two depths. For comparison, the results for two less attenuative models with damping factors 0.9995 and 0.9998, respectively, are also included. For each model, the quality factors are essentially constant across the array at the same depth. However, Q values measured at the free surface are systematically smaller than those measured at 10 km. Also, the γ values at 2 Hz are slightly smaller than those of 1 Hz. Nevertheless, it is clear that the Q we modeled can still be represented approximately as a linear function of frequency. Figures 8 through 10 show a set of amplitude spectra and the corresponding amplitude ratio for the anelastic model with a damping factor of 0.999. Over the frequency band 0.8-2.4 Hz, the ratio is rather flat.

Table 4. L_g Propagation in Anelastic Crustal Models

Damper	Sensor Location (km)		Results at 1 Hz			Results at 2 Hz		
G	Range	Depth	A/A_0	Q_0	γ (1 Hz)	A/A_0	Q(2 Hz)	γ (2 Hz)
0.9990	130	0	0.286	100	0.0096	0.351	239	0.0080
0.9990	140	0	0.262	100	0.0096	0.331	243	0.0079
0.9990	150	0	0.242	101	0.0095	0.293	232	0.0083
0.9990	160	0	0.230	104	0.0092	0.301	259	0.0074
0.9990	170	0	0.227	110	0.0087	0.300	276	0.0070
0.9990	180	0	0.201	108	0.0089	0.268	267	0.0072
0.9990	130	10	0.352	120	0.0080	0.377	251	0.0076
0.9990	140	10	0.316	116	0.0082	0.359	261	0.0073
0.9990	150	10	0.298	119	0.0081	0.333	261	0.0073
0.9990	160	10	0.284	122	0.0079	0.309	262	0.0073
0.9990	170	10	0.274	126	0.0076	0.289	262	0.0073
0.9990	180	10	0.252	125	0.0077	0.259	253	0.0076
0.9995	130	0	0.489	174	0.0055	0.555	420	0.0046
0.9995	140	0	0.460	173	0.0055	0.538	433	0.0044
0.9995	150	0	0.441	176	0.0055	0.499	403	0.0048
0.9995	160	0	0.440	187	0.0051	0.526	486	0.0039
0.9995	170	0	0.438	198	0.0048	0.534	537	0.0036
0.9995	180	0	0.410	194	0.0049	0.505	516	0.0037
0.9995	130	10	0.589	235	0.0041	0.601	474	0.0040
0.9995	140	10	0.551	225	0.0043	0.591	502	0.0038
0.9995	150	10	0.535	230	0.0042	0.566	500	0.0038
0.9995	160	10	0.526	239	0.0040	0.545	507	0.0038
0.9995	170	10	0.525	253	0.0038	0.523	496	0.0039
0.9995	180	10	0.495	246	0.0039	0.482	462	0.0041
0.9998	130	0	0.669	310	0.0031	0.730	772	0.0025
0.9998	140	0	0.644	305	0.0031	0.719	808	0.0024
0.9998	150	0	0.625	306	0.0031	0.682	714	0.0027
0.9998	160	0	0.642	347	0.0028	0.736	1034	0.0019
0.9998	170	0	0.649	378	0.0025	0.759	1272	0.0015
0.9998	180	0	0.620	362	0.0026	0.729	1135	0.0017
0.9998	130	10	0.799	556	0.0017	0.793	992	0.0019
0.9998	140	10	0.764	500	0.0019	0.794	1106	0.0017
0.9998	150	10	0.755	512	0.0019	0.776	1095	0.0018
0.9998	160	10	0.757	552	0.0017	0.762	1135	0.0017
0.9998	170	10	0.768	617	0.0016	0.741	1053	0.0018
0.9998	180	10	0.741	574	0.0017	0.698	910	0.0021

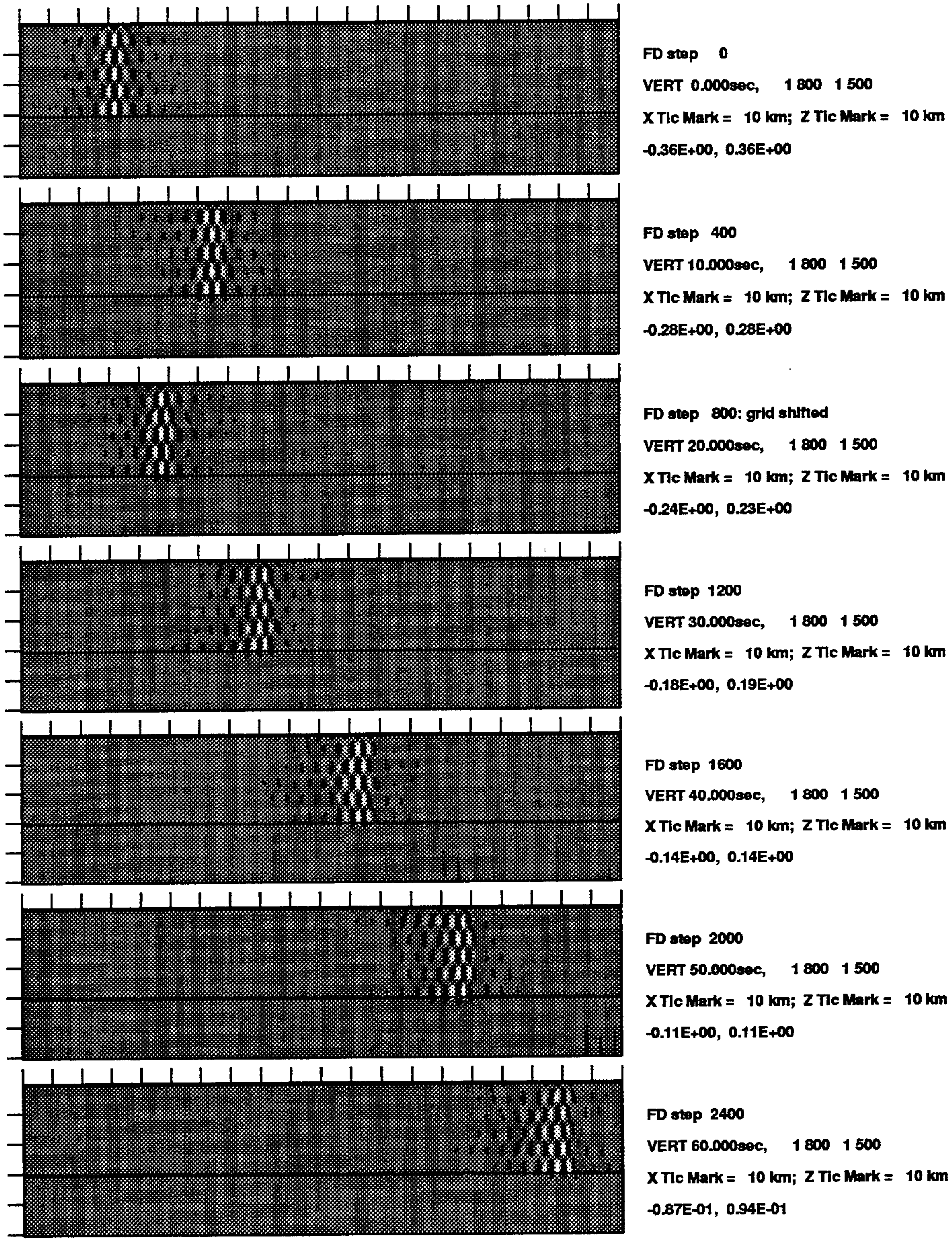

LFD Simulation of Lg Propagation: Model Q.999

Figure 5. The vertical-component snapshots of L_g wave propagation in an 1-layer anelastic crustal model. The maximum amplitude of the wavefield (shown at the right) drops from 0.360 to 0.094 after traveling a distance of 200 km. The chessboard-like pattern of the L_g wave packet, which is due to the constructive interference of multiply reflected planar S waves in the crust, is retained, however.

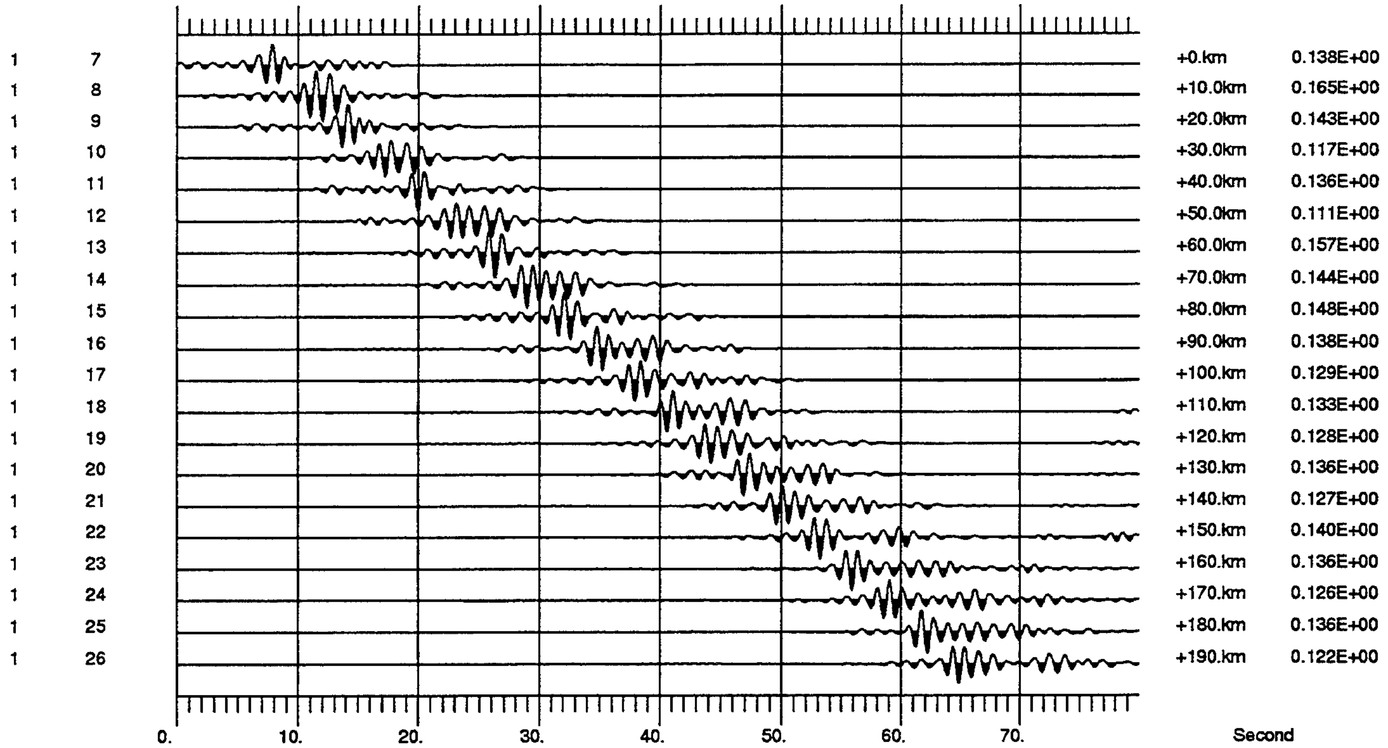

Lg in 1-layer Model without Q, Z Sensor Depth=0 km

VERT, same scale, decimated by 3

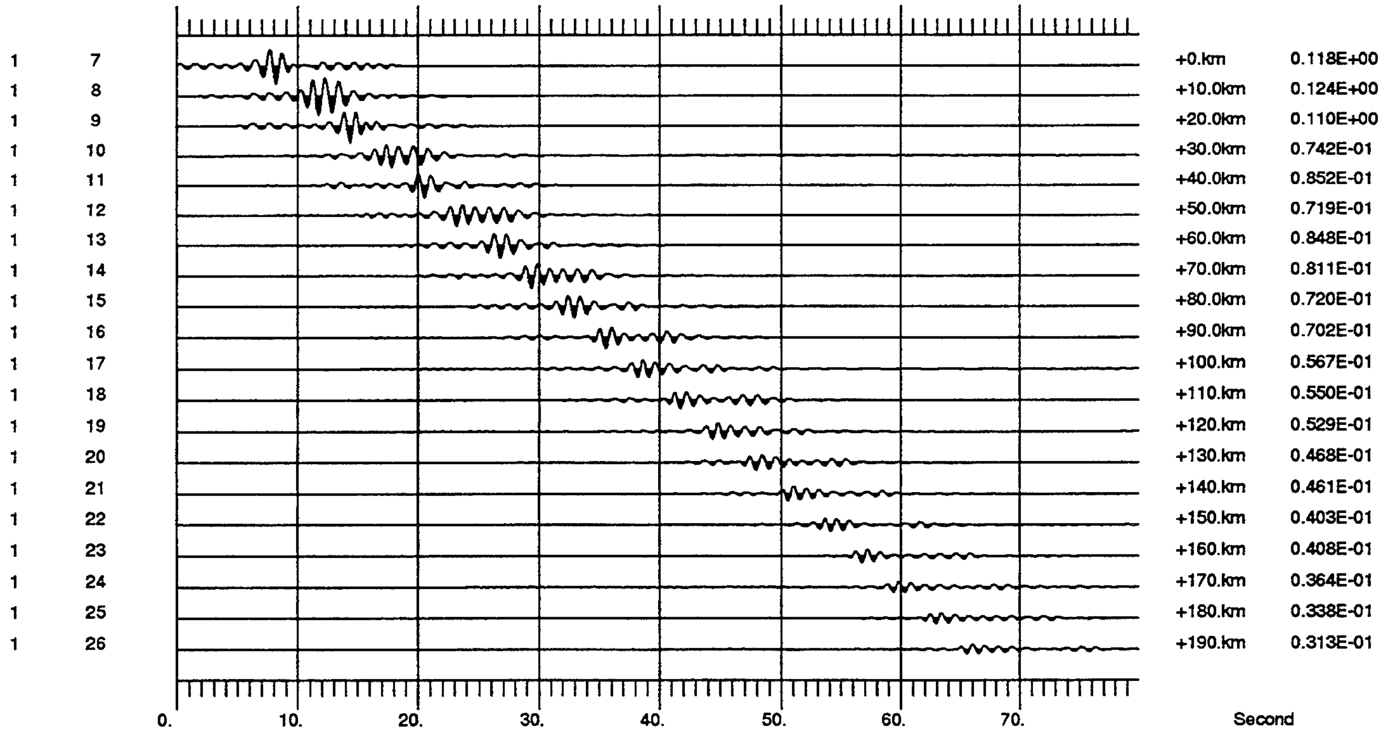

Lg in 1-layer Model with Q.999, Z Sensor Depth=0 km

VERT, same scale, decimated by 3

Figure 6. Vertical-component record sections of planar L_g wave propagation recorded at surface sensors (10 km apart) for the 1-layer elastic (top) and anelastic (bottom) crustal models, respectively.

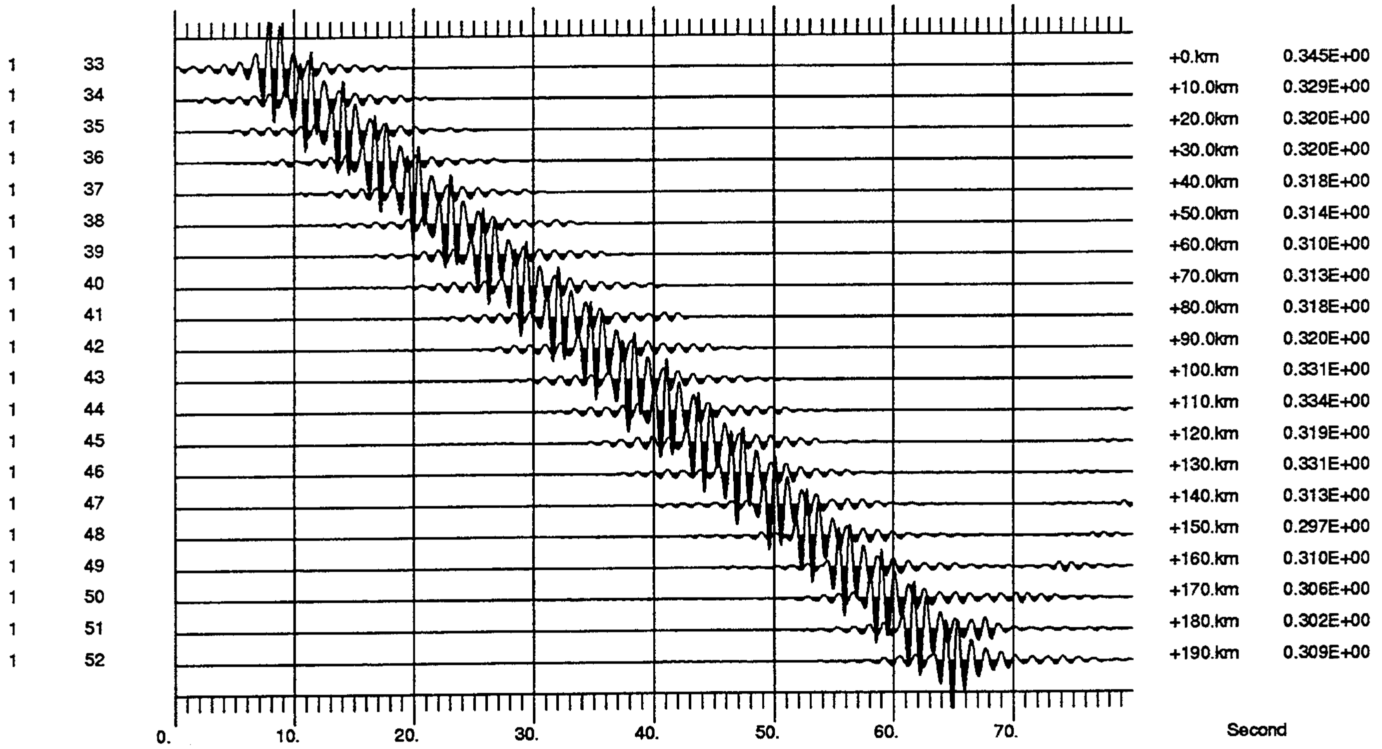

Lg in 1-layer Model without Q, Z Sensor Depth=10 km

VERT, same scale, decimated by 3

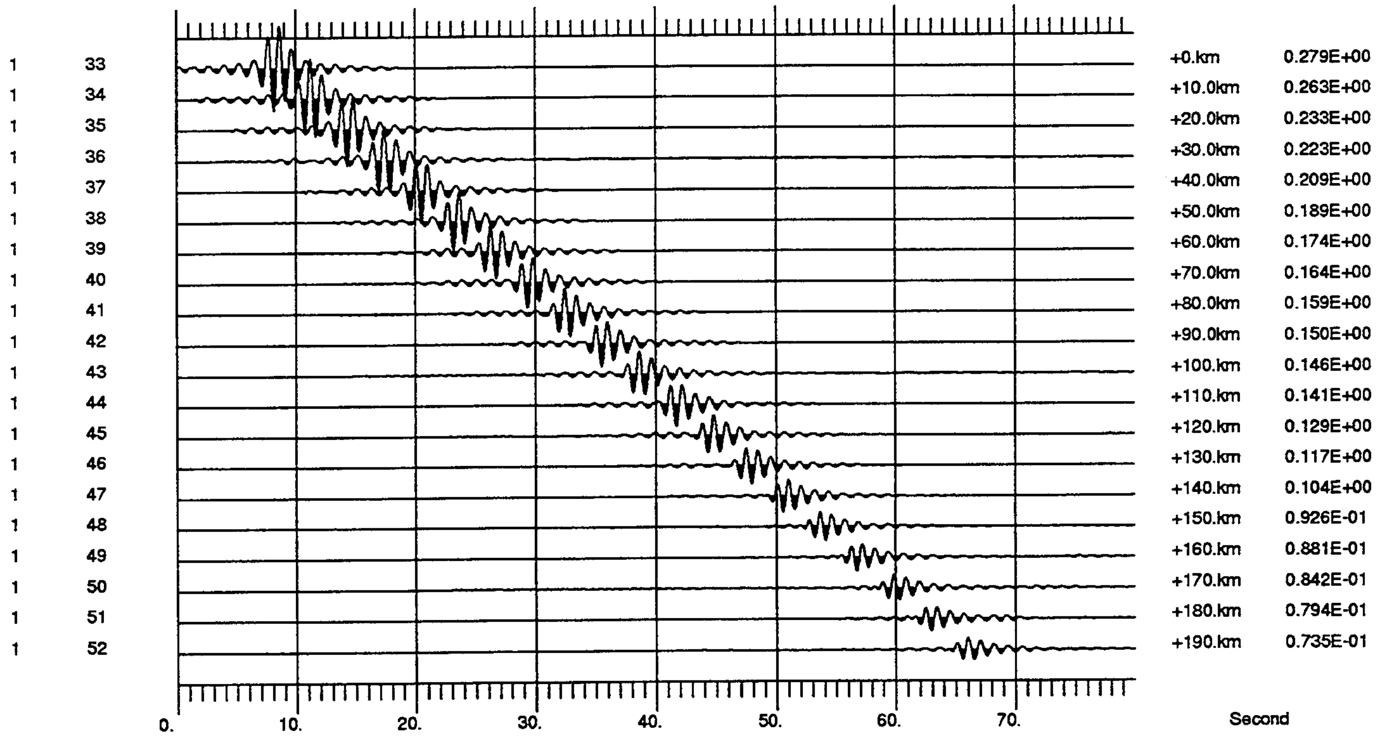

Lg in 1-layer Model with Q.999, Z Sensor Depth=10 km

VERT, same scale, decimated by 3

Figure 7. Vertical-component record sections of planar L_g waves recorded at sensors 10 km deep for the 1-layer elastic (top) and anelastic (bottom) crustal models, respectively. Parameters measured off synthetics at this depth, such as the peak amplitude and the group velocity, are more reliable than those measured at the free surface.

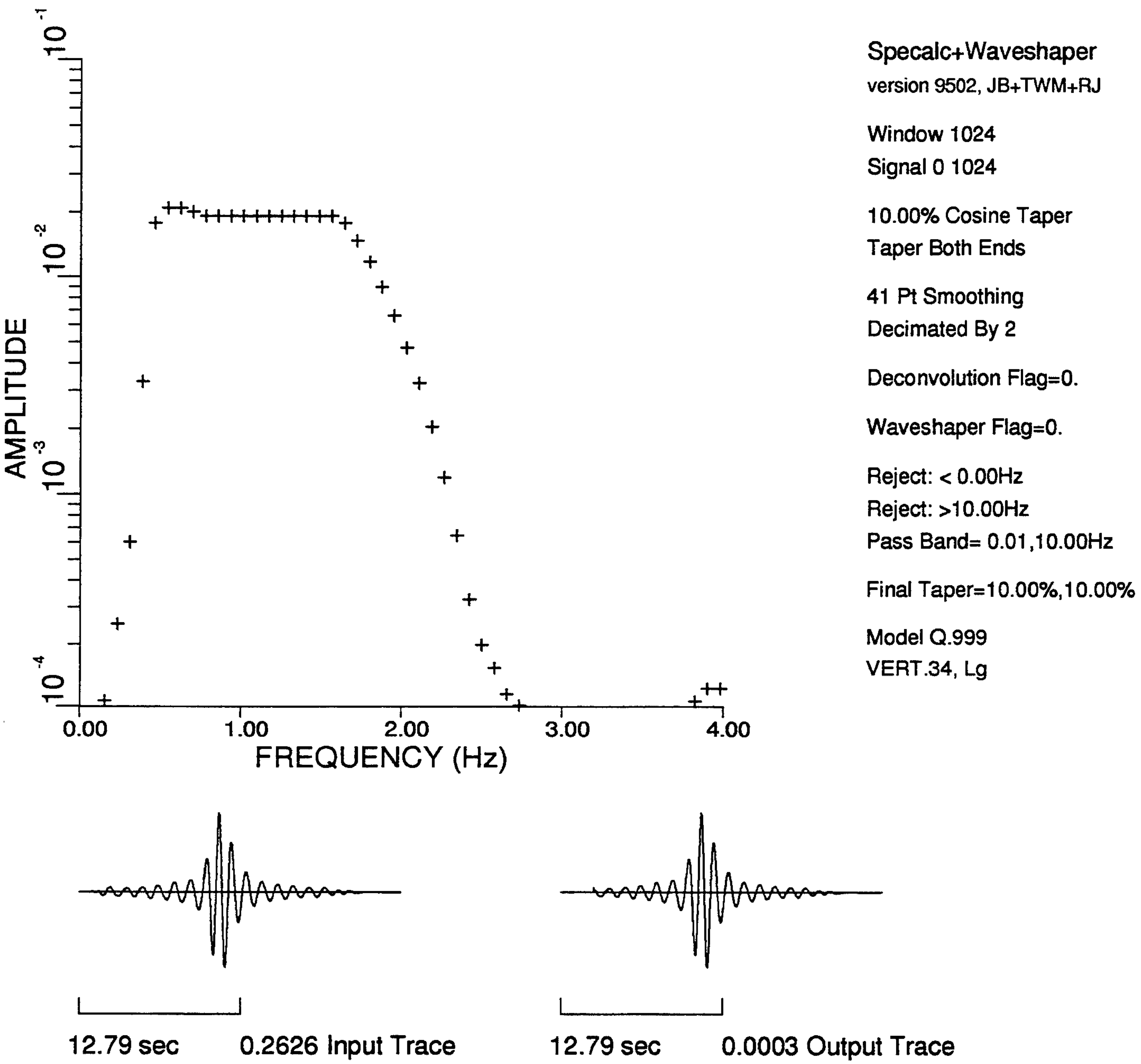

Specalc+Waveshaper
version 9502, JB+TWM+RJ

Window 1024
Signal 0 1024

10.00% Cosine Taper
Taper Both Ends

41 Pt Smoothing
Decimated By 2

Deconvolution Flag=0.

Waveshaper Flag=0.

Reject: < 0.00Hz
Reject: >10.00Hz
Pass Band= 0.01,10.00Hz

Final Taper=10.00%,10.00%

Model Q.999
VERT.34, Lg

Figure 8. Amplitude spectrum of the vertical-component displacement recorded at sensor No. 34 of the anelastic model. The sensor is located near the left portion of the grid, at a depth of 10 km.

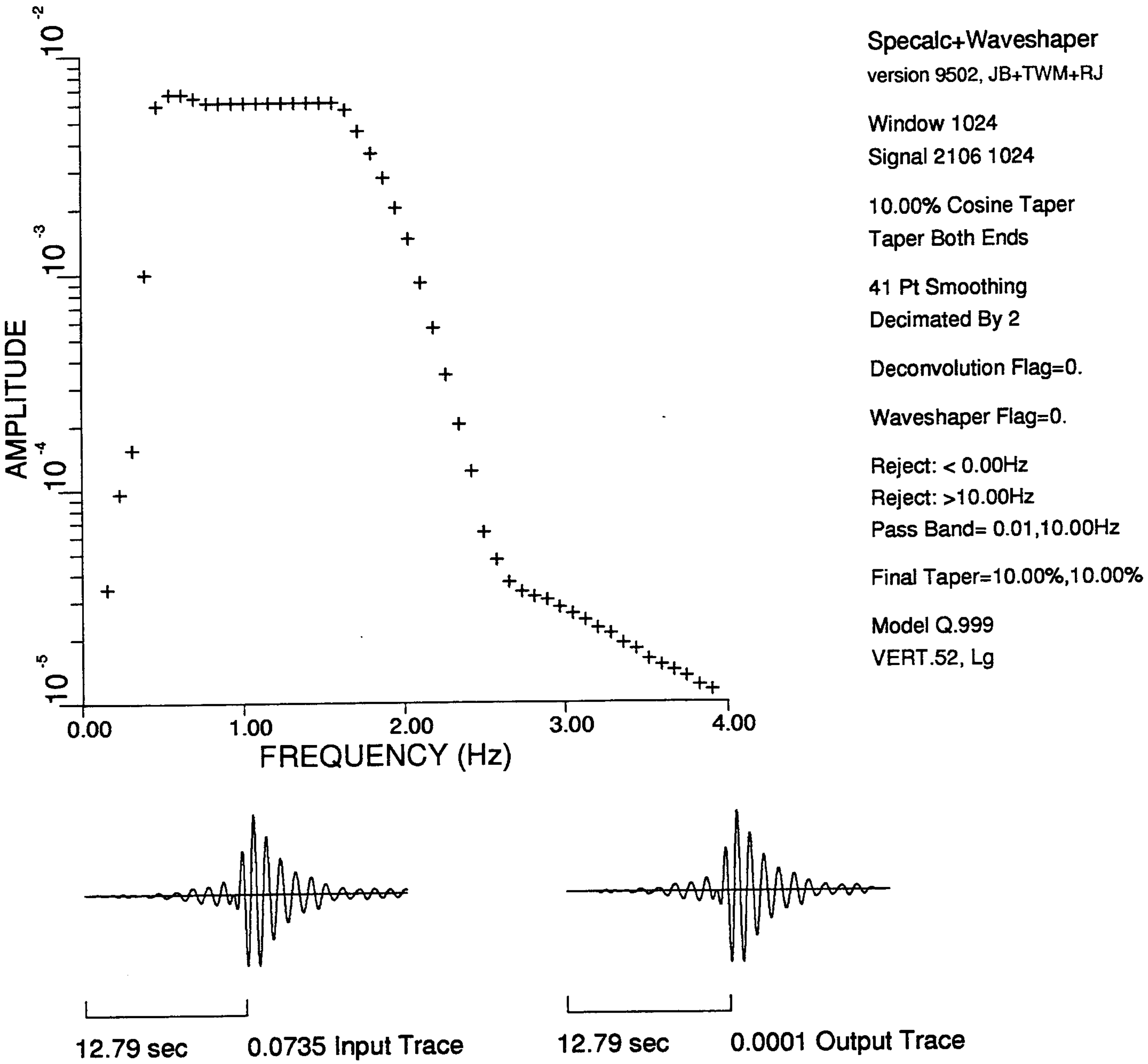

```
Specalc+Waveshaper
version 9502, JB+TWM+RJ

Window 1024
Signal 2106 1024

10.00% Cosine Taper
Taper Both Ends

41 Pt Smoothing
Decimated By 2

Deconvolution Flag=0.

Waveshaper Flag=0.

Reject: < 0.00Hz
Reject: >10.00Hz
Pass Band= 0.01,10.00Hz

Final Taper=10.00%,10.00%

Model Q.999
VERT.52, Lg
```

Figure 9. Amplitude spectrum of the vertical-component displacement recorded at sensor No. 52 of the anelastic model. The sensor is located near the right portion of the grid, at a depth of 10 km.

```
TGAL RATIO  vers 1.5 (JB+TWM+RAW+RJ)

Thu Nov  9 08:20:03 1995

Model Q.999, ratio: No.52 / No.34

NOISE POWER NOT SUBTRACTED FROM SIGNAL POWER

S/N POWER THRESHOLD = 2.0

7 POINT SMOOTHING
```

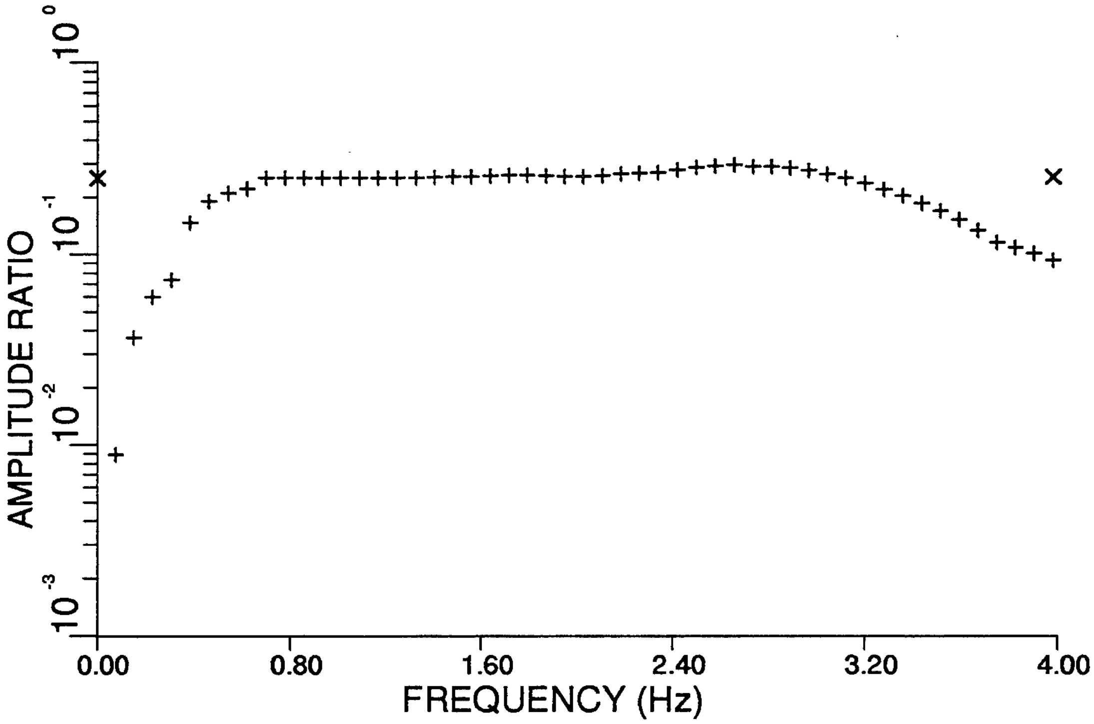

```
FREQ BAND  SLOPE      +/-        Y INTERC   AV INTEG    AV RATIO    SD
0.75-1.25  8.689e-04  3.475e-04  2.515e-01  -5.985e-01  -5.985e-01  1.993e-04
1.75-2.25  6.625e-03  1.528e-02  2.509e-01  -5.872e-01  -5.872e-01  5.559e-03
1.00-2.00  1.479e-02  2.644e-03  2.427e-01  -5.927e-01  -5.930e-01  5.356e-03
2.00-3.00  5.150e-02  1.182e-02  2.051e-01  -5.593e-01  -5.593e-01  2.034e-02
0.80-2.40  1.554e-02  2.074e-03  2.424e-01  -5.906e-01  -5.906e-01  8.369e-03
```

Figure 10. L_g amplitude ratio of synthetic seismograms No. 52 to No. 34 of the anelastic model. The sensors are 180 km apart (see Figures 7, 8, and 9). The amplitude ratio is nearly a constant of 0.24 over a rather broad band.

5. EXAMPLE 3: Rg-WAVE EXPERIMENT

Recent observational studies indicate that R_g could play an important role in L_g excitation for Yucca Flat explosions (Patton and Taylor, 1995). Numerical experiments by McLaughlin and Jih (1986, 1987) and Jih (1993b, 1995) readily demonstrate that rough topography and random heterogeneity can scatter significant R_g energy into body waves. An additional R_g–to–L_g conversion mechanism has just been reported (Jih, 1995). This new L_g excitation mechanism is rather interesting and worth some discussion here. It might be anticipated intuitively that the net effect of anelasticity in the surface layers is solely to reduce the amplitude of incident seismic waves. The R_g wave is particularly susceptible to such a mechanism since it is confined in the uppermost crustal layers where the anelastic attenuation is often very strong. However, if the anelastic attenuating layer is only thick enough to dissipate the retrograde rolling near the surface, then the free surface would behave asymptotically like a fixed point. Beyond a certain distance, the fundamental mode can no longer be sustained by such a waveguide, and accordingly any undissipated R_g energy would have to propagate in other wave types or modes. This is very similar to the situation of a solid half space with a rigid surface. There is no corresponding fundamental mode Rayleigh wave in such a structure (Aki and Richards, 1980, pp.189). Jih (1995) shows that this process couples the undissipated R_g energy into pure shear waves or higher modes, depending on the complexity of the structure. In terms of the R_g–to–S to R_g–to–P ratio, this process appears to be far more efficient than other near-surface R_g scattering mechanisms. Furthermore, in this process, the R_g spectrum is naturally imprinted onto the converted S waves, which could help to explain some recently observed spectral characteristics of L_g waves.

Two LFD experiments have been conducted here to illustrate these R_g–related findings. The first model is an anelastic half space with compressional and shear velocities of 5.02 and 2.898 km/sec, respectively. The damping factor is set to 0.9995 at every grid point. The vertical-component snapshots of R_g wave propagation in this anelastic half space are shown in Figure 11. Figure 12 shows vertical-component record sections of planar R_g waves recorded at surface sensors (top) and 5-km depth (bottom) for this anelastic half space model. The R_g energy is confined in the near-surface layer and very little energy is detected at a depth of 5 km, as expected. The fastest R_g phase has a group velocity of 2.33 km/sec, which is slower than that of R_g in the elastic case (Figure 12). The slowest R_g phase has a velocity of only about 1 km/sec (Figure 11). Figures 13 and 14 show the amplitude spectra of traces No. 5 and No. 20, respectively. These two surface sensors are 15 km apart. The spectral ratio is very flat over the frequency band between 2 and 10 Hz (Figure 15).

In the second test, all the parameters are identical to the first one except that the low-Q layer is limited to the uppermost 500 meters only (see Figure 16). Due to this peculiar structure, some R_g energy starts to detach from the Rayleigh mode and eventually is converted into primarily pure shear waves. These shear waves propagate at a post-critical angle and hence they are excellent candidates for regional shear phases such as S_g, L_g or L_g coda. Figure 17 shows the vertical-component record sections recorded at the free surface (top) and at 5-km depth (bottom) for this hybrid model. The converted shear waves (recorded at a depth of 5 km) have peak amplitudes actually greater than those of Rayleigh waves recorded at the surface sensors. It is also interesting to note that, while the R_g wave train travels at a velocity of 2.58 km/sec along the free surface, the converted shear waves have a velocity about 3.3 km/sec. This provides yet another piece of evidence that the converted shear waves are good candidates for the L_g-type of phase. Figures 18 through 20 show the spectra and ratio of traces No. 5 and No. 20 for this hybrid model. A synthetic seismogram recorded at 5-km depth is compared against the reference surface sensor No. 5 (Figures 21 and 22). All the spectral analysis and Q results are summarized in Table 5 below. Even though the same damping factor of 0.9995 was used in these two experiments, the resulting Q values, and the shape of transmitted R_g waves, as well as the wave field, all look very different. Apparently the thickness of the attenuating layer is very important. This is particularly true for R_g waves.

However, it should be emphasized that the role of anelastic attenuation in this new R_g–to–SVL_g conversion mechanism is to alter the eigenfunction corresponding to this peculiar structure, through dissipation of R_g energy near the free surface. The low Q layer itself does not preserve energy, nor does it re-direct any energy to escape from the layer. It is the energy in the R_g root, which was originally rolling underneath the top layer and was never dissipated by the absorption mechanism on the top, that eventually becomes detached from the energy trapped in the top layer. The energy in the R_g root is preserved and converted to S or L_g. Therefore, this R_g–to–S or R_g–to–L_g mechanism should be regarded as a mixture of absorption and scattering.

Table 5. R_g Propagation in Anelastic Crustal Models

Damper	Sensor Location (km)		Results at 2 Hz			Results at 4 Hz		
G, Thickness (km)	Range	Depth	A/A_0	Q(2 Hz)	γ (2 Hz)	A/A_0	Q(4 Hz)	γ (4 Hz)
0.9995, ∞	9	0	0.729	63	0.0420	0.729	150	0.0351
0.9995, ∞	10	0	0.691	62	0.0422	0.692	143	0.0368
0.9995, ∞	11	0	0.655	60	0.0438	0.656	138	0.0383
0.9995, ∞	12	0	0.620	56	0.0469	0.621	133	0.0397
0.9995, ∞	13	0	0.587	56	0.0469	0.588	129	0.0408
0.9995, ∞	14	0	0.557	57	0.0465	0.559	127	0.0416
0.9995, ∞	15	0	0.527	54	0.0485	0.529	124	0.0424
0.9995, ∞	16	0	0.498	53	0.0500	0.501	122	0.0432
0.9995, ∞	17	0	0.473	54	0.0486	0.476	121	0.0437
0.9995, ∞	18	0	0.454	54	0.0487	0.457	121	0.0435
0.9995, 0.5	9	0	0.543	26	0.0931	0.555	73	0.0653
0.9995, 0.5	10	0	0.513	26	0.0920	0.526	74	0.0642
0.9995, 0.5	11	0	0.487	26	0.0903	0.501	76	0.0628
0.9995, 0.5	12	0	0.464	27	0.0885	0.479	78	0.0614
0.9995, 0.5	13	0	0.444	28	0.0865	0.459	80	0.0598
0.9995, 0.5	14	0	0.426	28	0.0846	0.442	82	0.0584
0.9995, 0.5	15	0	0.410	29	0.0826	0.425	84	0.0570
0.9995, 0.5	16	0	0.395	30	0.0806	0.411	86	0.0556
0.9995, 0.5	17	0	0.381	30	0.0785	0.397	88	0.0544
0.9995, 0.5	18	0	0.366	31	0.0770	0.382	89	0.0534
0.9995, 0.5	9	5	0.243	14	0.1341	0.239	23	0.1590
0.9995, 0.5	10	5	0.282	17	0.1060	0.277	29	0.1283
0.9995, 0.5	11	5	0.311	21	0.0879	0.306	34	0.1077
0.9995, 0.5	12	5	0.330	24	0.0761	0.324	39	0.0938
0.9995, 0.5	13	5	0.340	27	0.0682	0.335	44	0.0842
0.9995, 0.5	14	5	0.346	29	0.0626	0.341	48	0.0770
0.9995, 0.5	15	5	0.348	32	0.0585	0.342	52	0.0715
0.9995, 0.5	16	5	0.346	33	0.0554	0.341	55	0.0673
0.9995, 0.5	17	5	0.343	35	0.0529	0.338	58	0.0638
0.9995, 0.5	18	5	0.338	36	0.0511	0.333	60	0.0611

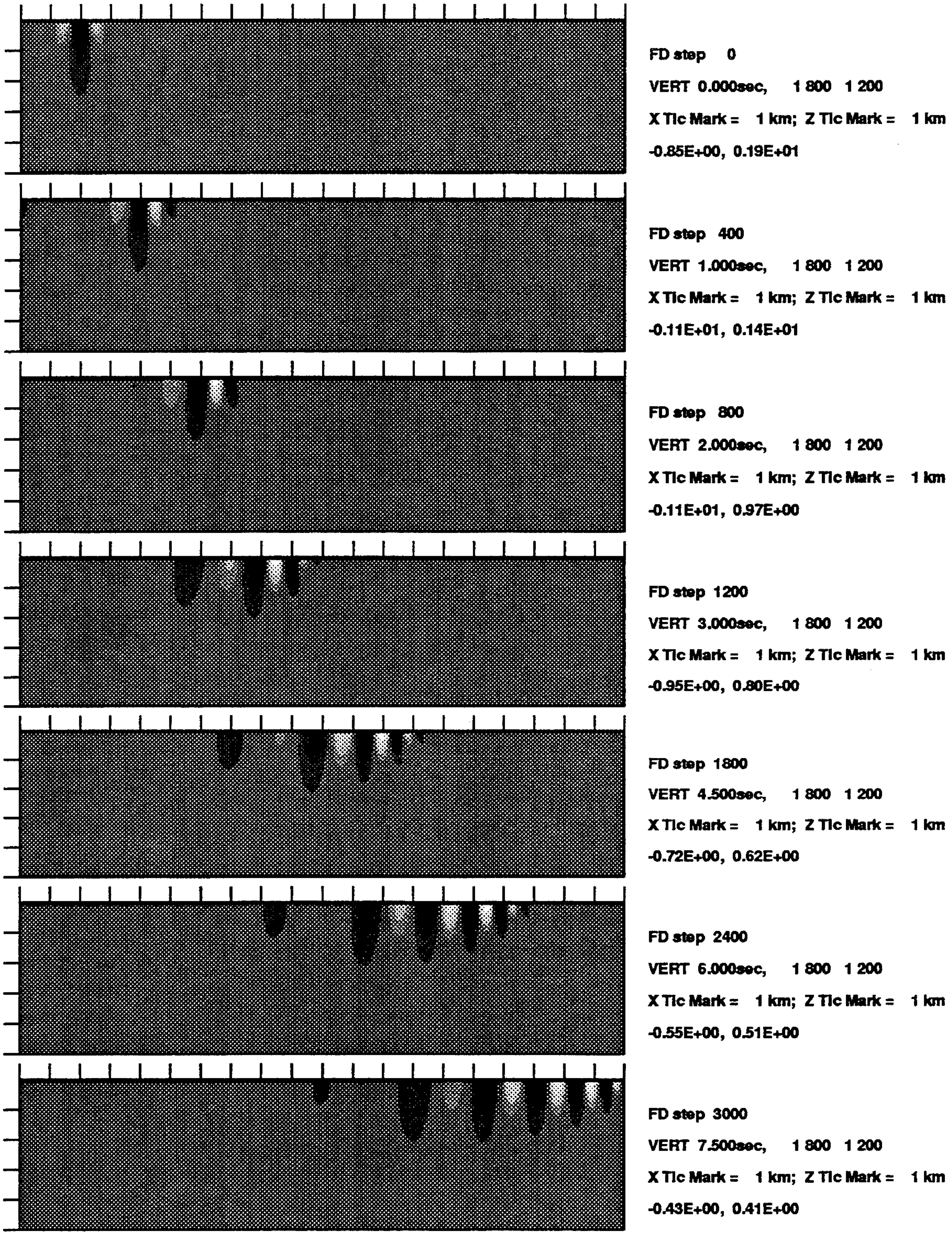

LFD Simulation of Rg Propagation: Model Q.9995,600

Figure 11. The vertical-component snapshots of R_g wave propagation in an anelastic half space. The compressional and shear velocities are 5.02 and 2.898 km/sec, respectively. The damping factor is 0.9995 at every grid point. The intrinsic attenuation in the half space causes a severe dispersion, which has been shown to be a necessary condition of causality.

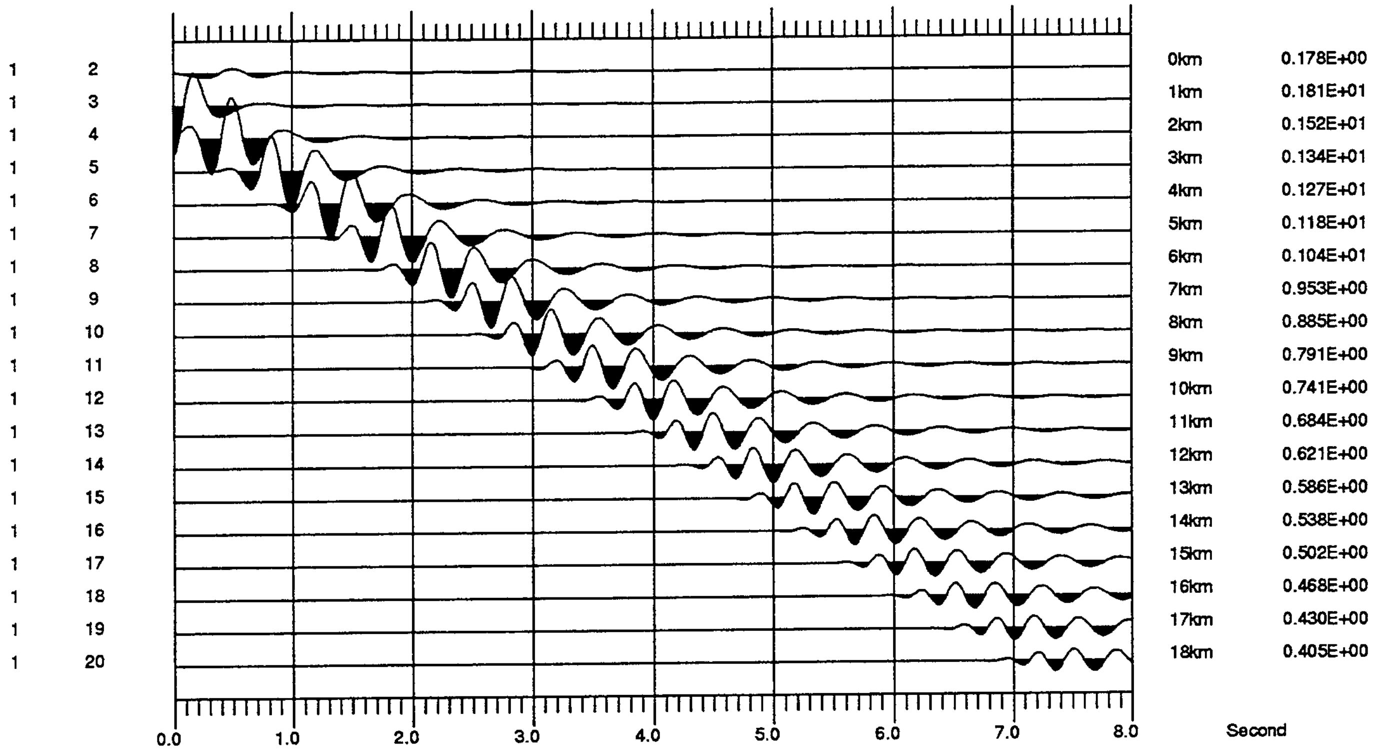

Rg+HS+Q; G(HS)=0.9995, Z component, sensor depth = 0km

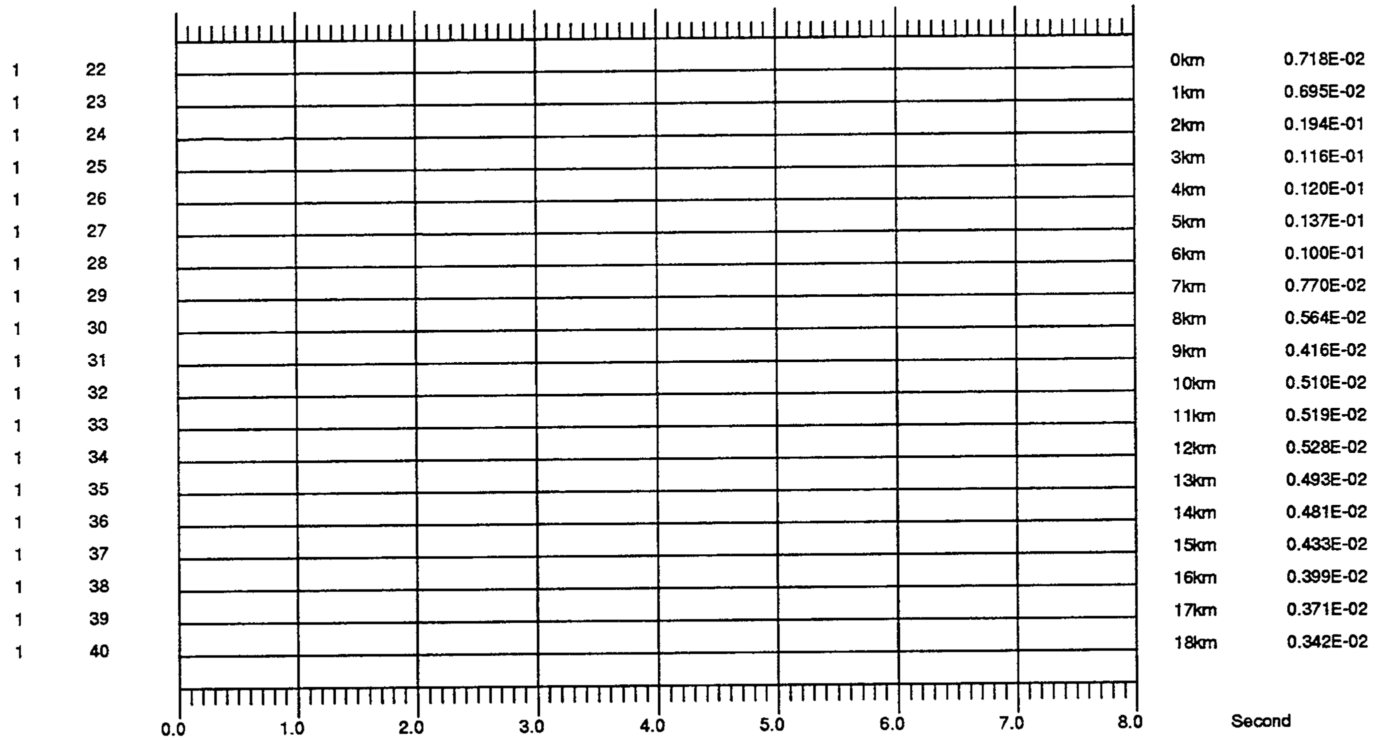

Rg+HS+Q; G(HS)=0.9995, Z component, sensor depth = 5km

Figure 12. Vertical-component record sections of planar R_g waves recorded at surface sensors (top) and 5-km depth (bottom) for the anelastic half space model. The R_g energy is confined in the near-surface layer and very little energy is detected at a depth of 5 km.

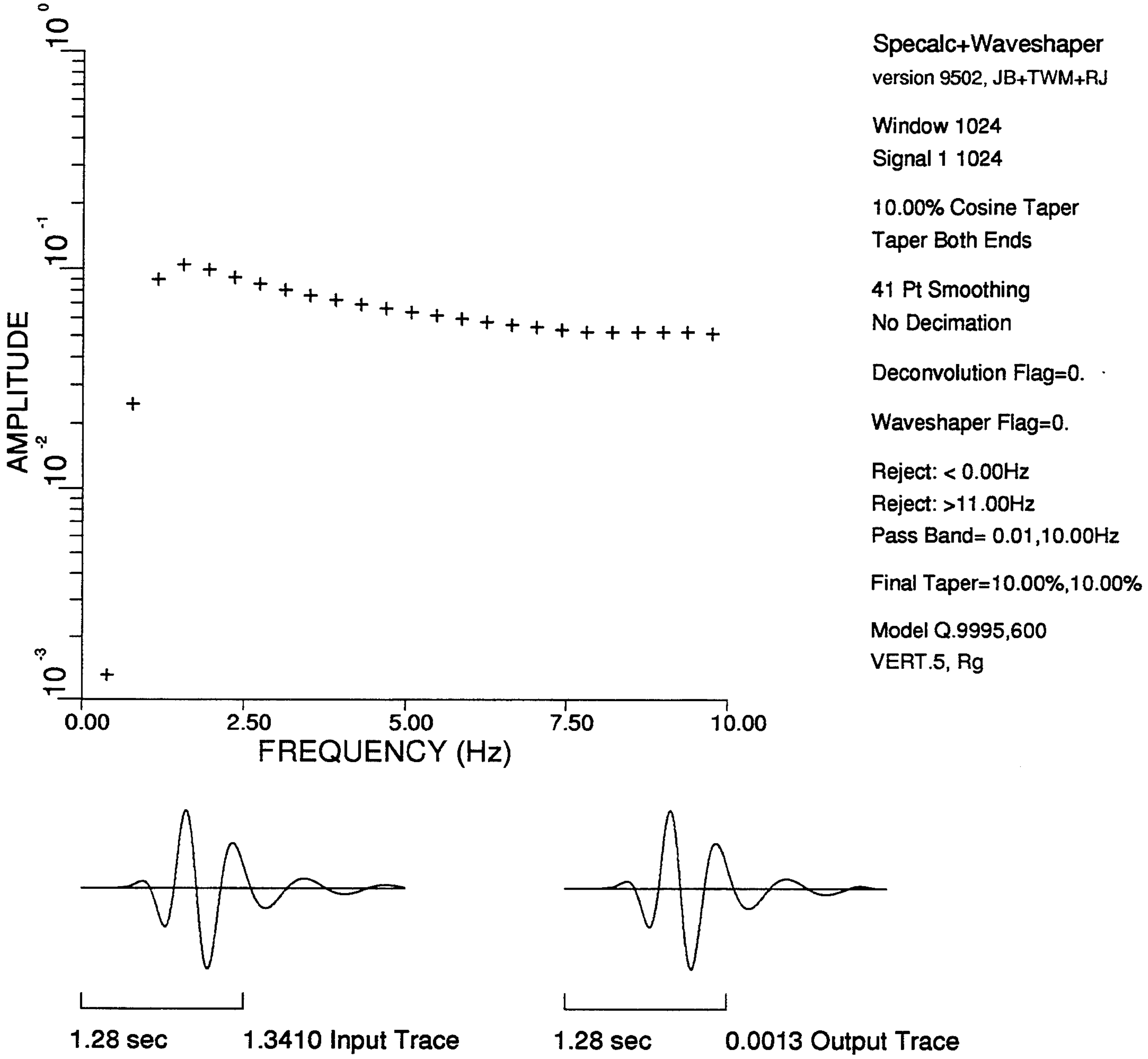

Specalc+Waveshaper
version 9502, JB+TWM+RJ

Window 1024
Signal 1 1024

10.00% Cosine Taper
Taper Both Ends

41 Pt Smoothing
No Decimation

Deconvolution Flag=0.

Waveshaper Flag=0.

Reject: < 0.00Hz
Reject: >11.00Hz
Pass Band= 0.01,10.00Hz

Final Taper=10.00%,10.00%

Model Q.9995,600
VERT.5, Rg

Figure 13. Amplitude spectrum of the vertical-component displacement recorded at sensor No. 5 of the anelastic half-space model with a damping factor of 0.9995. The sensor is located near the left portion of the grid.

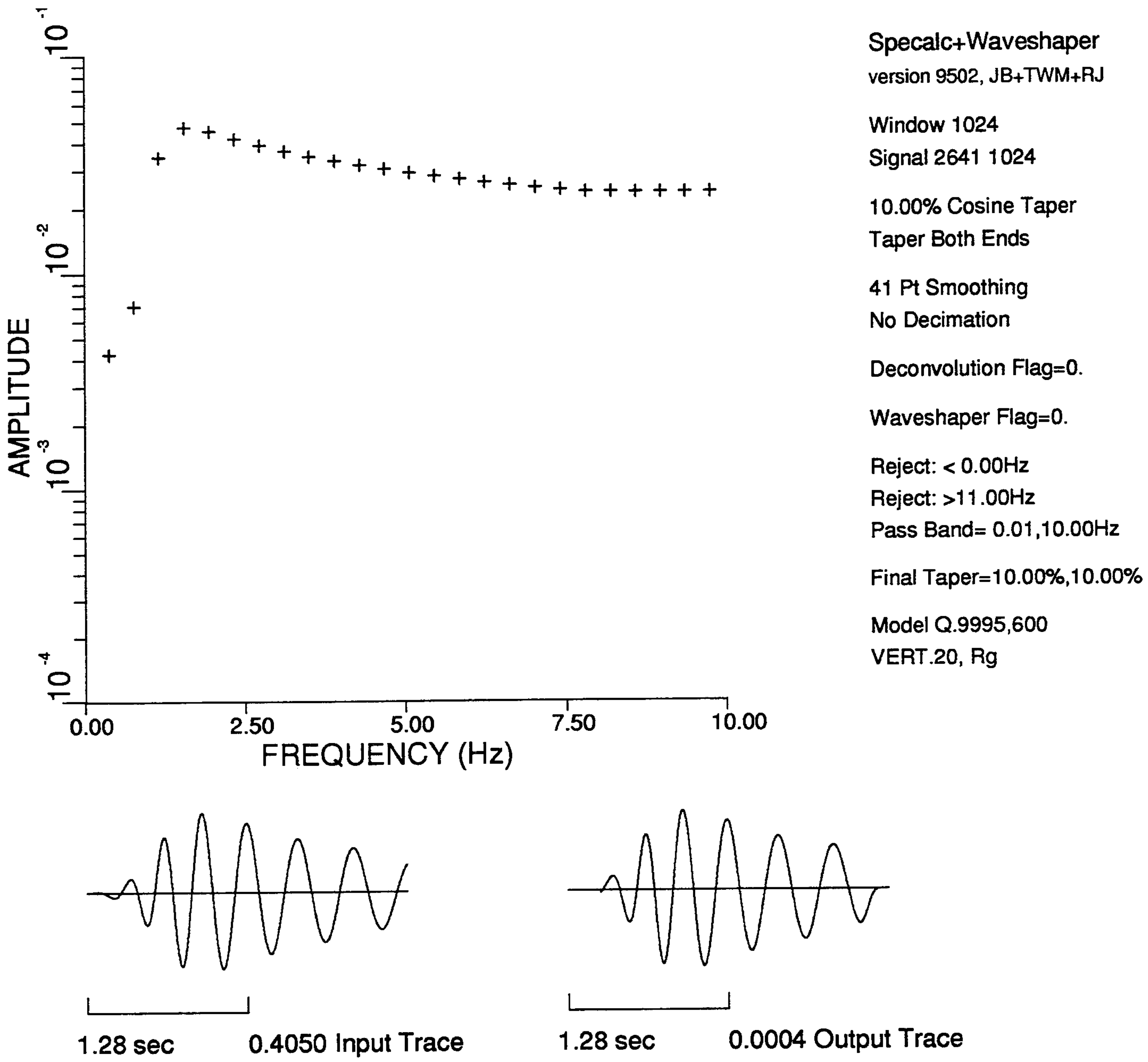

Specalc+Waveshaper
version 9502, JB+TWM+RJ

Window 1024
Signal 2641 1024

10.00% Cosine Taper
Taper Both Ends

41 Pt Smoothing
No Decimation

Deconvolution Flag=0.

Waveshaper Flag=0.

Reject: < 0.00Hz
Reject: >11.00Hz
Pass Band= 0.01,10.00Hz

Final Taper=10.00%,10.00%

Model Q.9995,600
VERT.20, Rg

Figure 14. Amplitude spectrum of the vertical-component displacement recorded at surface sensor No. 20 of the anelastic half-space model. The sensor is located near the right portion of the grid.

TGAL RATIO vers 1.5 (JB+TWM+RAW+RJ)

Fri Nov 10 09:44:02 1995

Model Q.9995,600, ratio: No.20 / No.5

NOISE POWER NOT SUBTRACTED FROM SIGNAL POWER

S/N POWER THRESHOLD = 2.0

7 POINT SMOOTHING

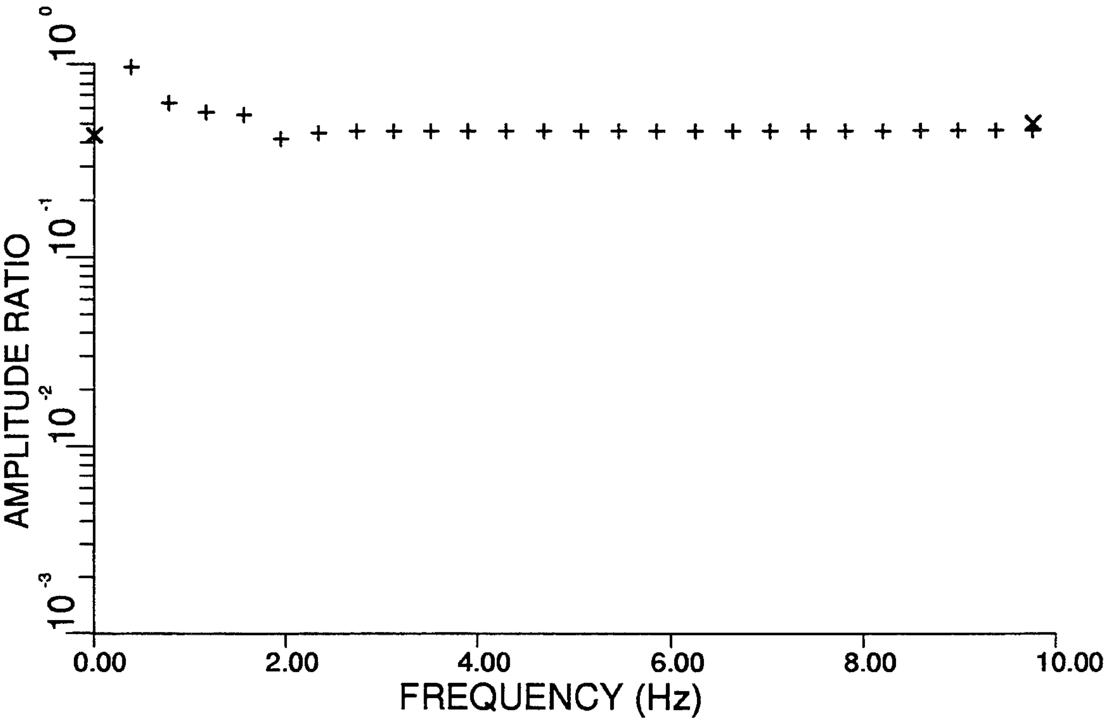

FREQ BAND	SLOPE	+/-	Y INTERC	AV INTEG	AV RATIO	SD
2.00-4.00	6.314e-03	2.437e-03	4.340e-01	-3.435e-01	-3.427e-01	5.153e-03
4.00-6.00	1.000e-06	1.245e-06	4.570e-01	-3.401e-01	-3.401e-01	0.000e+00
6.00-8.00	-8.350e-05	1.612e-05	4.575e-01	-3.402e-01	-3.402e-01	0.000e+00
3.00-8.00	-4.565e-06	8.843e-06	4.570e-01	-3.402e-01	-3.402e-01	1.410e-04
2.00-10.00	5.078e-04	2.300e-04	4.531e-01	-3.408e-01	-3.407e-01	2.651e-03

Figure 15. R_g amplitude ratio of synthetic seismograms No. 20 to No. 5 of the anelastic half-space model with a damping factor 0.9995. These two sensors are 15 km apart (see Figure 12).

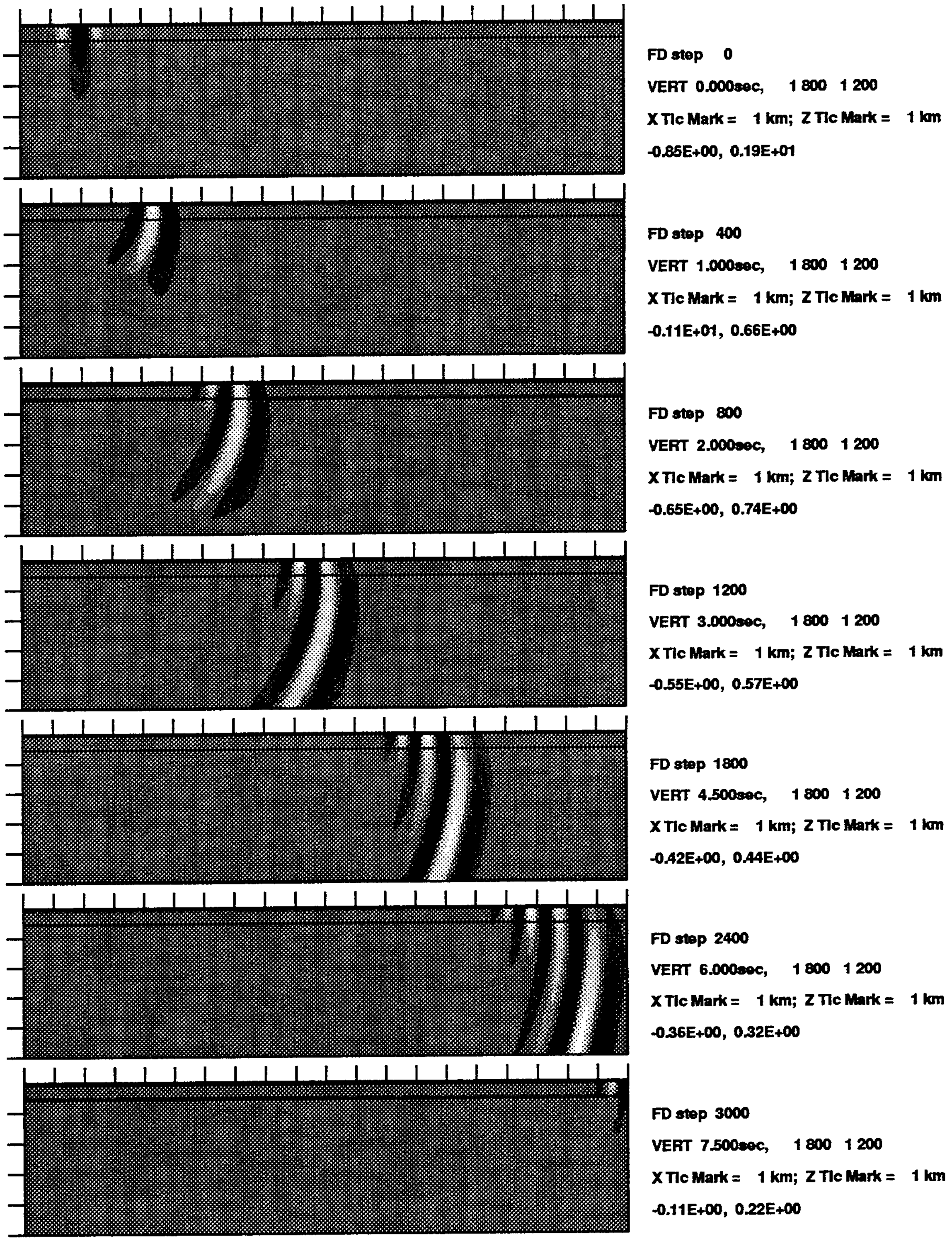

LFD Simulation of Rg Propagation: Model Q.9995,22

Figure 16. The vertical-component snapshots of R_g wave propagation in an elastic half space with an anelastic layer of 500 meters thick lying over it. Due to this peculiar structure, some R_g energy appears to have gradually detached from Rayleigh mode and been converted into primarily pure shear waves.

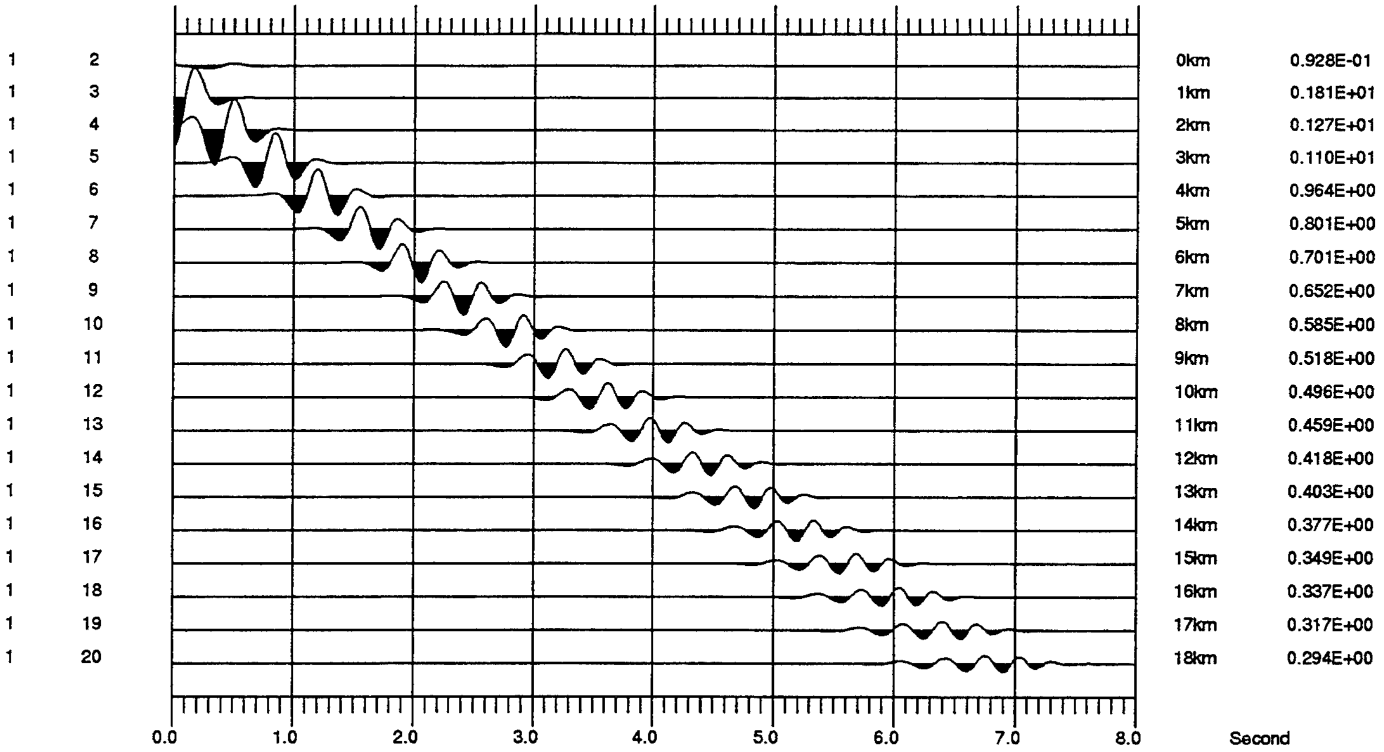

Rg+HS+Q; G(top 500m)=0.9995, Z component, sensor depth = 0km

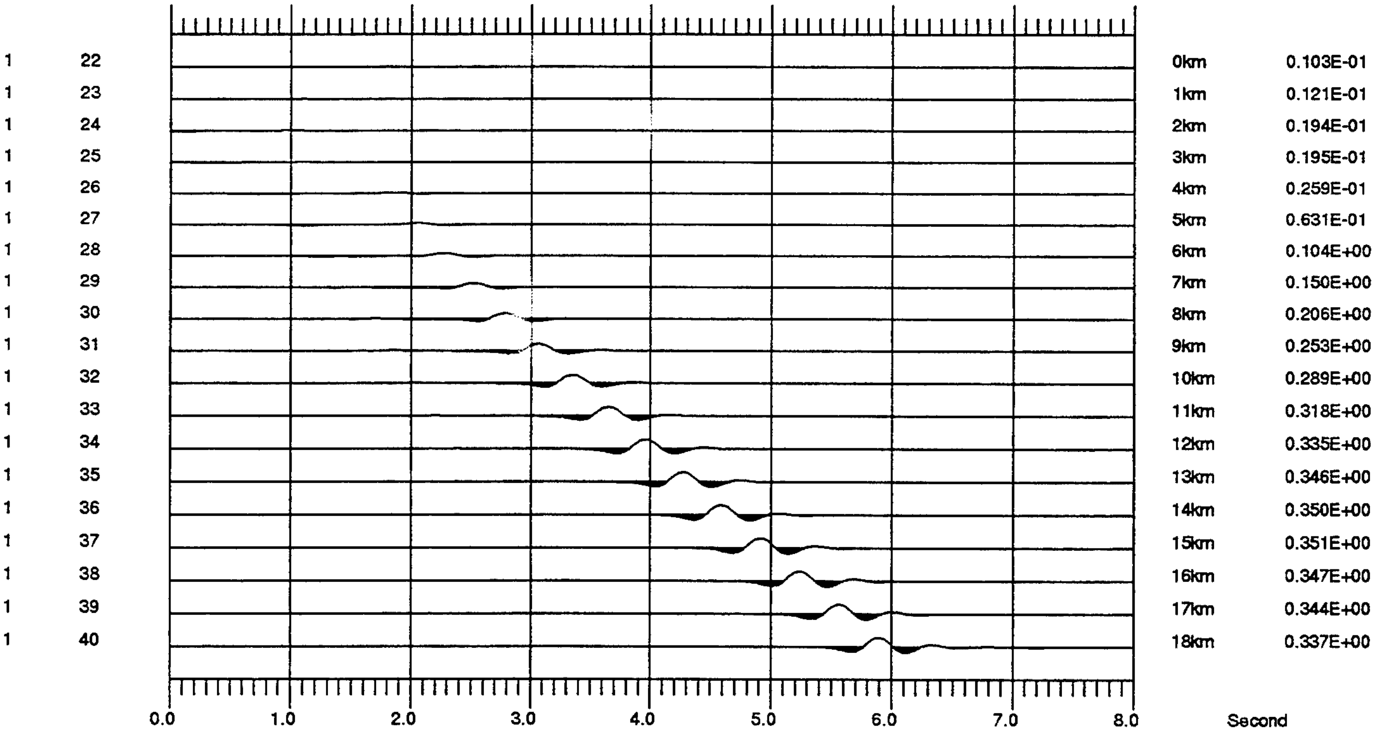

Rg+HS+Q; G(top 500m)=0.9995, Z component, sensor depth = 5km

Figure 17. Vertical-component record sections of planar R_g waves recorded at surface sensors (top) and 5-km depth (bottom) for the elastic half space with a shallow anelastic layer lying over it. The converted shear waves have peak amplitudes greater than those of Rayleigh waves recorded at the surface sensors.

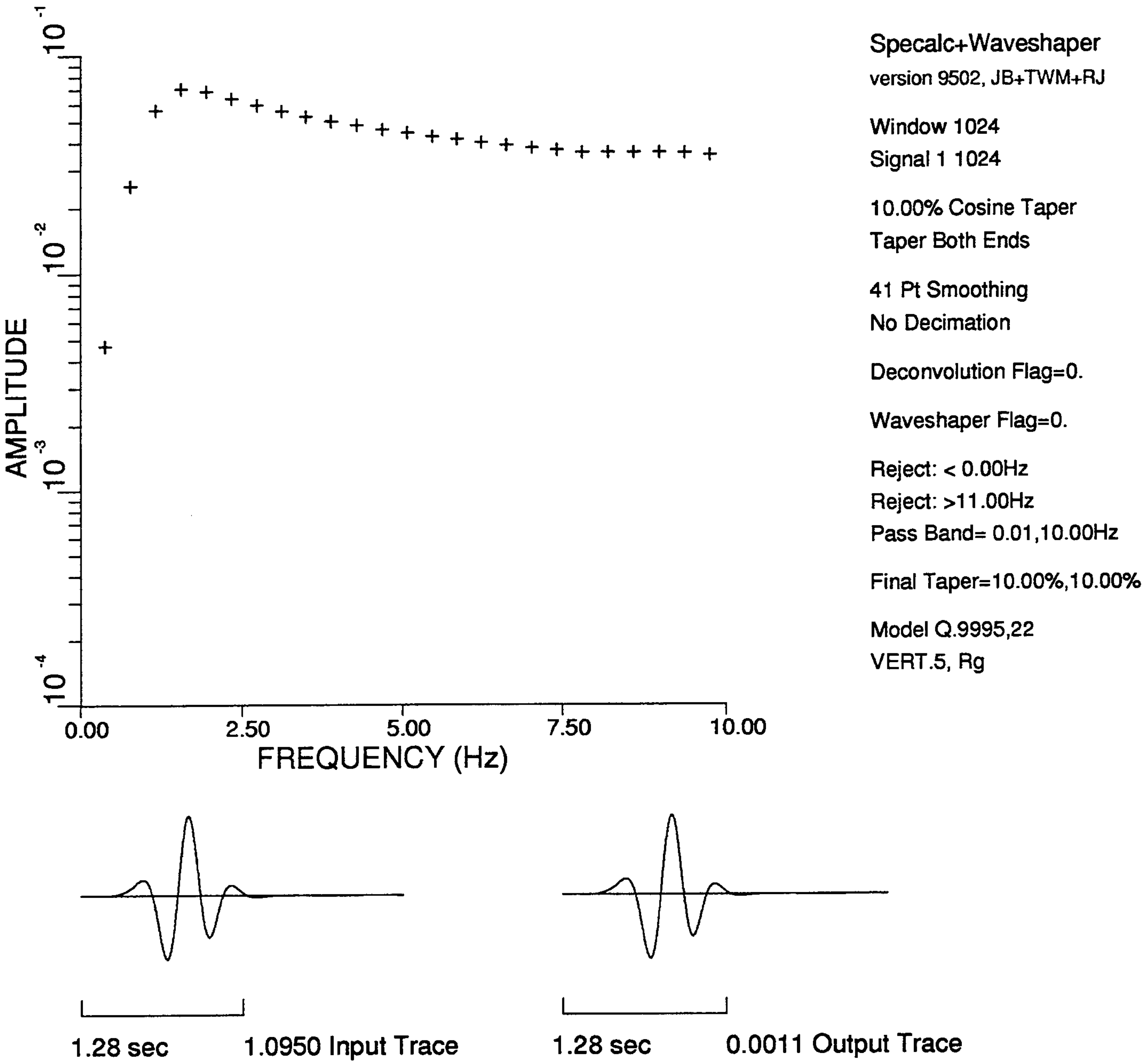

Specalc+Waveshaper
version 9502, JB+TWM+RJ

Window 1024
Signal 1 1024

10.00% Cosine Taper
Taper Both Ends

41 Pt Smoothing
No Decimation

Deconvolution Flag=0.

Waveshaper Flag=0.

Reject: < 0.00Hz
Reject: >11.00Hz
Pass Band= 0.01,10.00Hz

Final Taper=10.00%,10.00%

Model Q.9995,22
VERT.5, Rg

Figure 18. Amplitude spectrum of the vertical-component displacement recorded at sensor No. 5 of the anelastic model. This surface sensor is located near the left portion of the grid.

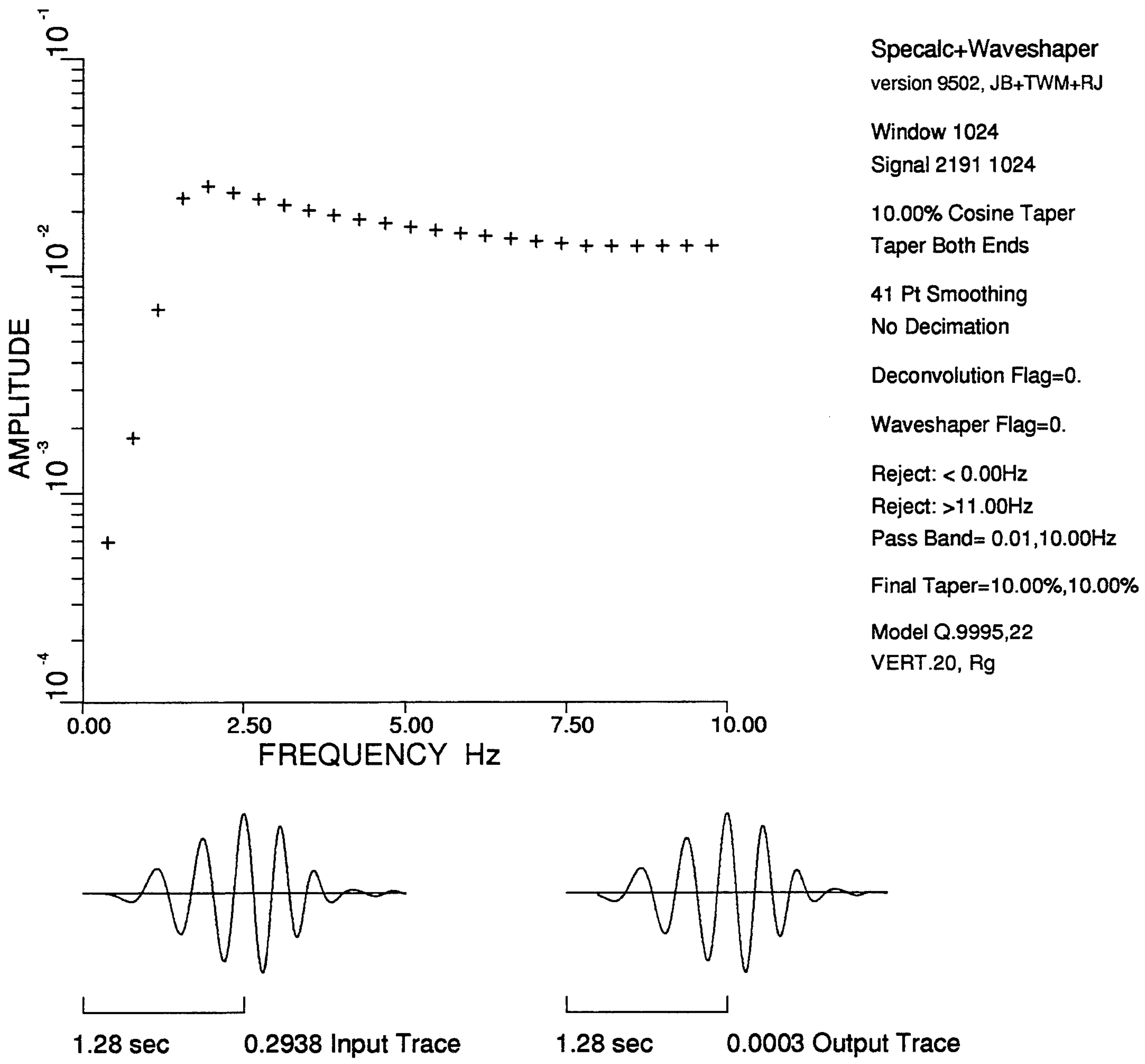

Specalc+Waveshaper
version 9502, JB+TWM+RJ

Window 1024
Signal 2191 1024

10.00% Cosine Taper
Taper Both Ends

41 Pt Smoothing
No Decimation

Deconvolution Flag=0.

Waveshaper Flag=0.

Reject: < 0.00Hz
Reject: >11.00Hz
Pass Band= 0.01,10.00Hz

Final Taper=10.00%,10.00%

Model Q.9995,22
VERT.20, Rg

Figure 19. Amplitude spectrum of the vertical-component displacement recorded at sensor No. 20 of the half-space model with a shallow attenuating layer lying over it. This surface sensor is located near the right portion of the grid.

TGAL RATIO vers 1.5 (JB+TWM+RAW+RJ)

Fri Nov 10 09:42:16 1995

Model Q.9995,22, ratio: No.20 / No.5

NOISE POWER NOT SUBTRACTED FROM SIGNAL POWER

S/N POWER THRESHOLD = 2.0

7 POINT SMOOTHING

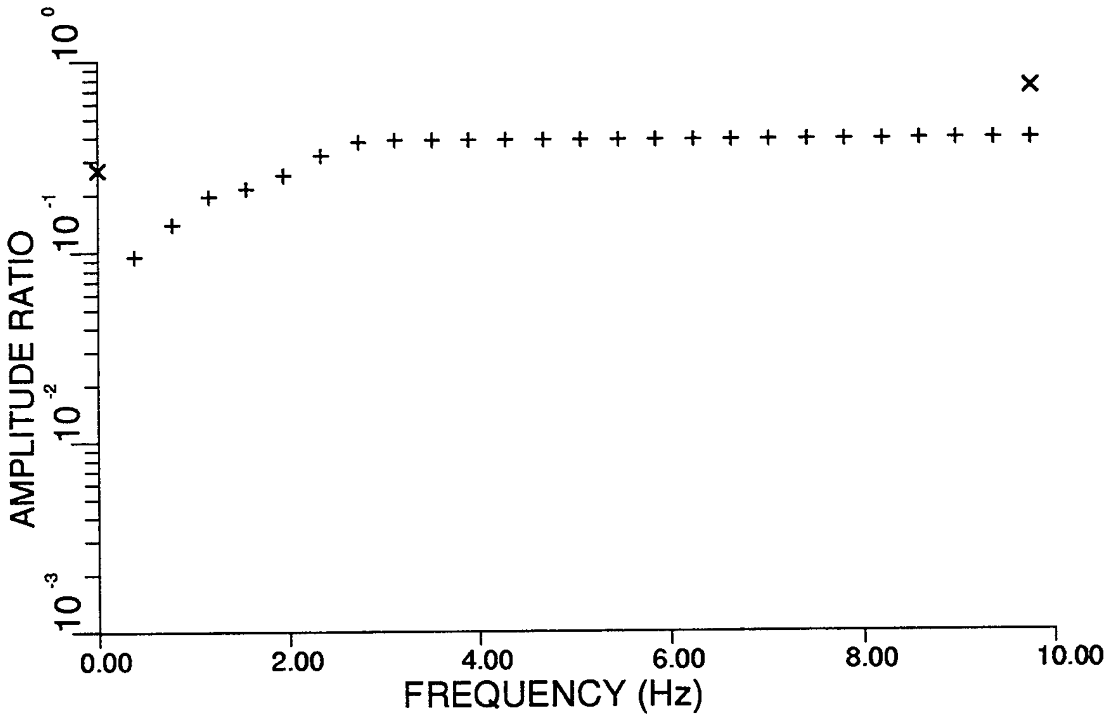

FREQ BAND	SLOPE	+/-	Y INTERC	AV INTEG	AV RATIO	SD
2.00-4.00	4.366e-02	1.601e-02	2.676e-01	-4.415e-01	-4.361e-01	3.487e-02
4.00-6.00	1.500e-06	1.327e-06	3.821e-01	-4.179e-01	-4.179e-01	NaN
6.00-8.00	1.800e-05	7.278e-06	3.820e-01	-4.178e-01	-4.178e-01	1.726e-04
3.00-8.00	5.249e-05	2.468e-05	3.818e-01	-4.179e-01	-4.179e-01	1.410e-04
2.00-10.00	3.675e-03	1.551e-03	3.597e-01	-4.220e-01	-4.218e-01	1.814e-02

Figure 20. R_g amplitude ratio of synthetic seismograms No. 20 to No. 5 of the anelastic half-space model. These two sensors are 15 km apart (see Figure 17).

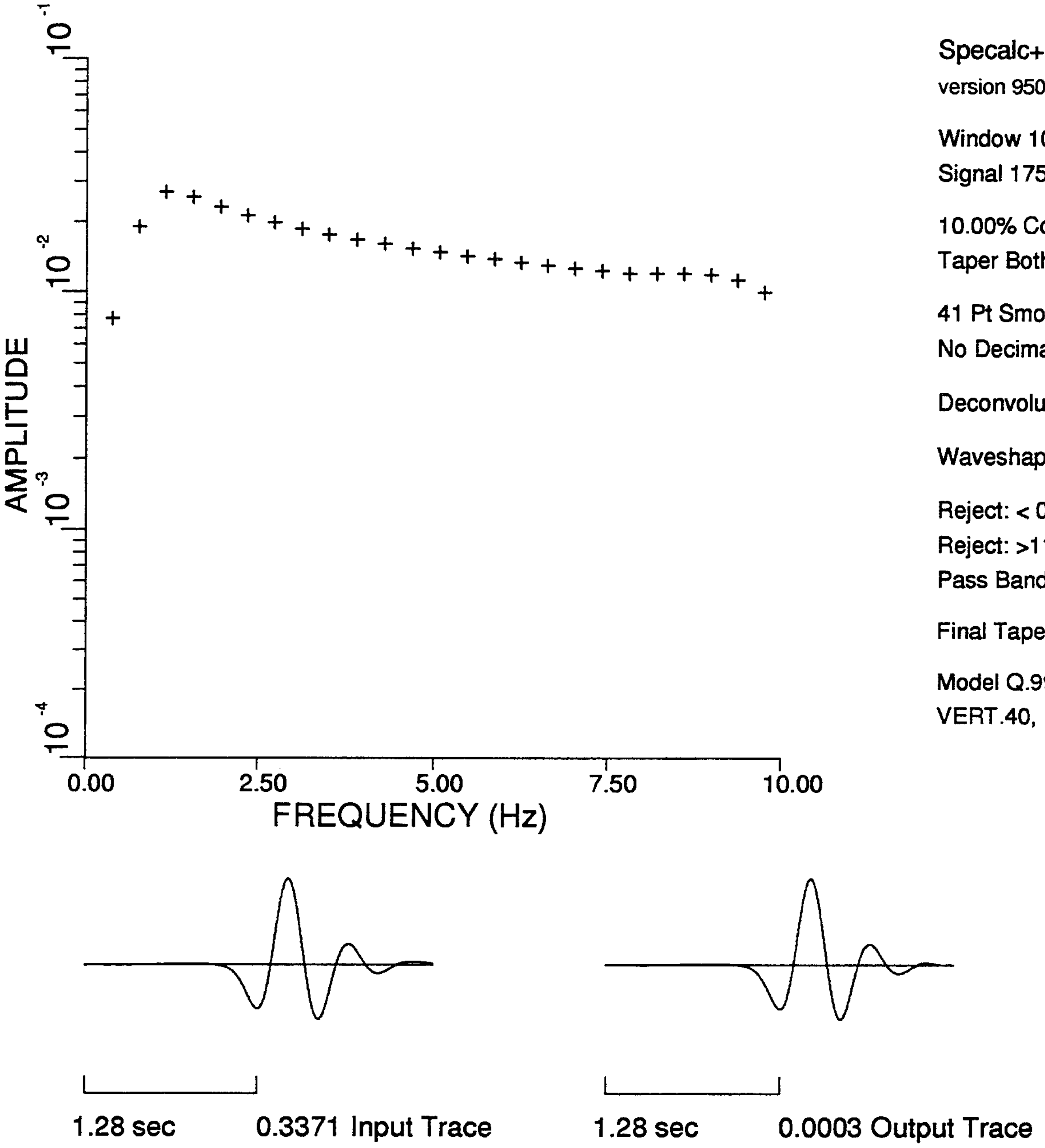

Specalc+Waveshaper
version 9502, JB+TWM+RJ

Window 1024
Signal 1756 1024

10.00% Cosine Taper
Taper Both Ends

41 Pt Smoothing
No Decimation

Deconvolution Flag=0.

Waveshaper Flag=0.

Reject: < 0.00Hz
Reject: >11.00Hz
Pass Band= 0.01,10.00Hz

Final Taper=10.00%,10.00%

Model Q.9995,22
VERT.40, Rg

Figure 21. Amplitude spectrum of the vertical-component displacement recorded at the sensor No. 40 of the half-space model with a shallow attenuating layer lying over it. This sensor is located near the right portion of the grid, at a depth of 5 km.

```
TGAL RATIO  vers 1.5 (JB+TWM+RAW+RJ)

Fri Nov 10 09:43:09 1995

Model Q.9995,22, ratio: No.40 / No.5

NOISE POWER NOT SUBTRACTED FROM SIGNAL POWER

S/N POWER THRESHOLD = 2.0

7 POINT SMOOTHING
```

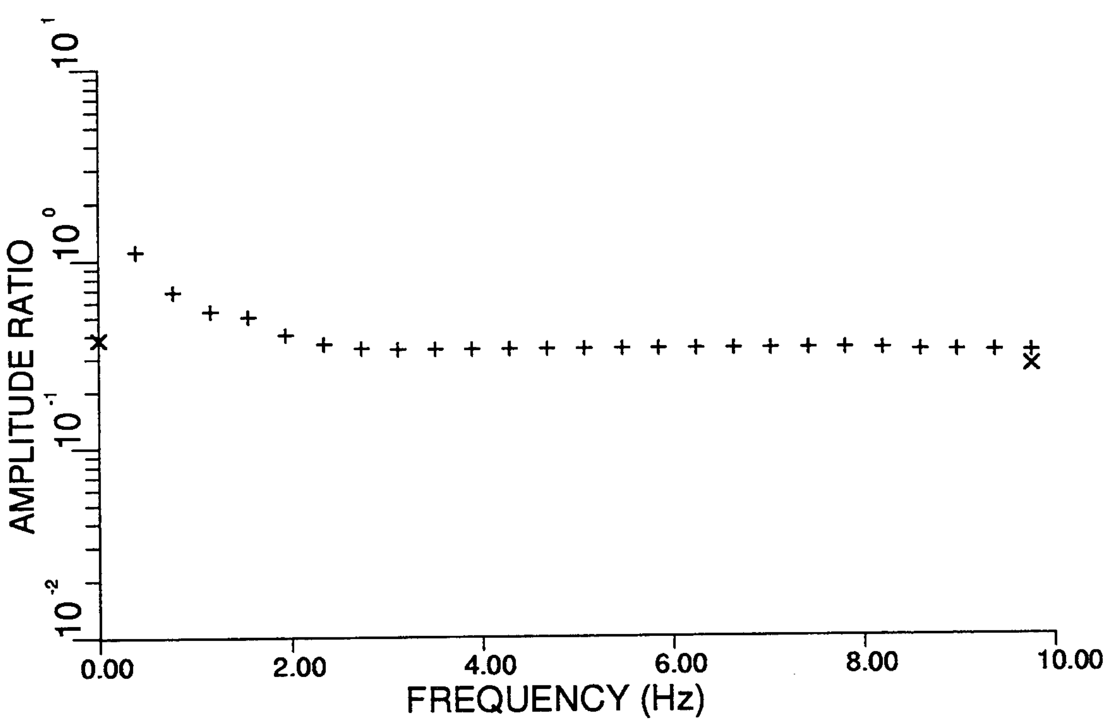

```
FREQ BAND    SLOPE      +/-      Y INTERC   AV INTEG   AV RATIO    SD
2.00-4.00   -1.563e-02  5.172e-03  3.785e-01  -4.688e-01  -4.708e-01  1.201e-02
4.00-6.00    1.500e-06  2.869e-06  3.330e-01  -4.775e-01  -4.775e-01  0.000e+00
6.00-8.00   -6.570e-04  2.051e-04  3.364e-01  -4.778e-01  -4.778e-01  4.883e-04
3.00-8.00   -1.600e-04  4.867e-05  3.336e-01  -4.776e-01  -4.776e-01  3.729e-04
2.00-10.00  -3.707e-03  6.229e-04  3.488e-01  -4.797e-01  -4.799e-01  1.072e-02
```

Figure 22. R_g amplitude ratio of synthetic seismograms No. 40 to No. 5 of the half-space model with a shallow attenuating layer lying over it. Trace No. 40 is 15 km away from the surface sensor No. 5. At a depth of 5 km, sensor No. 40 only records the converted shear waves that travel at a postcritical angle.

6. DISCUSSION AND CONCLUSION

A simple, causal method for incorporating anelastic attenuation into the LFD method is presented in this report. The method is simple to implement. Testing of this algorithm with various seismic waves demonstrates that this damping operator provides the expected intrinsic attenuation over a rather broad frequency band. This *ad hoc* damping gives an intrinsic attenuation with the quality factor increasing linearly with the frequency. Also, in the P-SV situation, the resulting Q_P and Q_S are approximately the same. If a frequency dependence other than the linear one is desired, then several separate finite-difference simulations need to be carried out for each individual frequency–Q pair of interest. The shortcomings of this procedure are outweighed by the simplicity. More importantly, this procedure preserves the causality. Using the algorithm described in this study, it is easier to relate and equate the propagation effects due to small-scale random heterogeneities (and other large-scale structural variations) with those due to the anelastic attenuation (see Jih, 1995, 1996).

The procedure described in this study is based on that of Cerjan *et al.* (1985). It is shown that this simple procedure results in an amplitude that decays exponentially with traveling distance, which happens to be an approximate solution to the telegraphy equation (Levander, 1985a). The damping effect added to the wave equation is equivalent to, at least asymptotically, the friction term Levander (1985a) added to the wave equation. Thus the empirical damping also has a theoretical justification. Since our damping term, G, is meant to represent the spatial attenuation, which is a very localized phenomenon, the damping term could vary from grid to grid. However, if it is used as a supplementary absorbing boundary condition, there may be a gradient in G that would provide a better effect (see Sochaki *et al.*, 1987).

All the examples tested in this study consistently show that, the performance of this damping procedure as an attenuation operator degrades somewhat at very low frequencies. There could be damping or amplification of the signal at the low frequency end, a phenomenon which Levander (1985a) also observed in utilizing the telegraphy equation as an auxiliary absorbing boundary. Nevertheless, as Levander (1985a) pointed out, the introduction of a low-frequency reflection (or amplification) is more desirable than a high-frequency reflection (or amplification). It is appropriate to regard this damping procedure (as well as Levander's use of the telegraphy equation) as an *ad hoc* measure, useful until a more robust attenuation operator or absorbing boundary condition is developed.

REFERENCES

Aki, K. and P. Richards (1980). *Quantitative Seismology: Theory and Methods, Voulme 1,* W. H. Freeman and Company, San Francisco, CA.

Bache, T. C., H. Swanger, and B. Shekoller (1981). *Synthesis of L_g in Eastern Uhited States crustal models with frequency independent Q,* Report SSS-R-81-4668, S-Cubed, La Jolla, CA.

Boore, D. (1970). Love waves in nonuniform wave guides: finite-difference calculations, *J. Geophy. Res.,* **75,** 1512-1527,

Cerjan, C., D. Kosloff, R. Kosloff, and M. Reshef (1985). A nonreflecting boundary condition for discrete acoustic and elastic wave equations, *Geophysics,* **50,** 705-708.

Day, S. M. and J. B. Minster (1984). Numerical simulation of wavefields using a Pade approximation method, *Geophys. J. R. astr. Soc.,* **78,** 105-118.

Emmerich, H. and M. Korn (1987). Incorporation of attenuation into time-domain computation of seismic wave fields, *Geophysics,* **52,** 1252-1264.

Frankel, A. and L. Wennerberg (1987). Energy-flux model of seismic coda: separation of scattering and intrinsic attenuation, *Bull. Seism. Soc. Am.,* **77,** 1223-1251.

Futterman, W. I. (1962). Dispersive body waves, *J. Geophys. Res.,* **69,** 5279-5291.

Ganley, D. C. (1981). A method for calculating synthetic seismograms which include the effects of absorption and dispersion, *Geophysics,* **46,** 1100-1107.

Jacobson, R. S. (1987). An investigation into the fundamental relationship between attenuation, phase dispersion, and frequency using seismic refraction profiles over sedimentary structures, *Geophysics,* **52,** 72-87.

Jih, R.-S. (1993a). *User's manual of FD2: a software package for modeling seismological problems with 2-dimensional linear finite-difference method,* Report TGAL-93-06, Teledyne Geotech, Alexandria, VA.

Jih, R.-S. (1993b). *Statistical characterization of rugged propagation paths with application to R_g scattering study,* Report TGAL-93-07, Teledyne Geotech, Alexandria, VA.

Jih, R.-S. (1995). Numerical investigation of relative contributions of R_g scattering and attenuation to L_g excitation, in *Proceedings of 17th PL/AFOSR Seismic Research Symposium* (12-15 Sept 1995, Scottsdale, AZ; J. Lewkowicz, J. McPhetres, and D. Reiter eds.), Report PL-TR-95-2108, Phillips Laboratory, Hanscom AFB, MA, pp. 401-410.

Jih, R.-S. (1996). *Waveguide effects of large-scale structural variation, anelastic attenuation, and random heterogeneity on SV L_g propagation: a finite-difference modeling study,* Report PL-TR-96-2016, Phillips Laboratory, Hanscom AFB, MA.

Levander, A. (1985a). Use of the telegraphy equation to improve absorbing boundary efficiency for fourth-order acoustic wave finite-difference schemes, *Bull. Seism. Soc. Am.,* **75,** 1847-1852.

Levander, A. (1985b). Finite-difference calculations of dispersive Rayleigh wave propagation, *Tectonophysics,* **113,** 1-30.

Liu, H. P., D. L. Anderson, and H. Kanamori (1976). Velocity dispersion due to anelasticity: implications for seismology and mantle composition, *Geophys. J. R. astr. Soc.*, **47,** 41-58.

McLaughlin, K. L. and R.-S. Jih (1986). *Finite-difference simulations of Rayleigh wave scattering by 2-D rough topography,* Report AFGL-TR-86-0269 (=TGAL-86-09), Air Force Geophysics Laboratory, Hanscom AFB, MA (ADA 179190).

McLaughlin, K. L. and R.-S. Jih (1987). *Finite-difference simulations of Rayleigh wave scattering by shallow heterogeneity,* Report AFGL-TR-87-0322 (=TGAL-87-02), Air Force Geophysics Laboratory, Hanscom AFB, MA (ADA 194961).

Minster, J. B., S. M. Day, and P. M. Shearer (1991). The transition to the elastic regime in the vicinity of an underground explosion, in *Explosion Source Phenomenology, (AGU Geophysical Monograph Volume 65,* S. Taylor, H. Patton, and P. Richards eds.), Amer. Geophys. U., Washington DC, pp. 229-238.

Patton, H. J. and S. R. Taylor (1995). Analysis of L_g spectral ratios from NTS explosions: implications for the source mechanisms of spall and the generation of L_g waves, *Bull. Seism. Soc. Am.,* **85,** 220-236.

Sochaki, J., R. Kubichek, J. George, W. R. Fletcher, and S. Smithson (1987). Absorbing boundary conditions and surface waves, *Geophysics,* **52,** 60-71.

Toksoz, M. N., A. M. Dainty, and E. E. Charrette (1986). *Development of ultrasonic modeling techniques for the study of seismic wave scattering due to crustal inhomogeneities,* Report AFGL-TR-86-0078, Air Force Geophysics Laboratory, Hanscom AFB, MA (ADA 170062).

Vidale, J. and D. V. Helmberger (1988). Elastic finite-difference modeling of the 1971 San Fernando, California, earthquake, *Bull. Seism. Soc. Am.,* **78,** 122-141.

DISTRIBUTION LIST

NON-GOVERNMENT RECIPIENTS

Prof. Thomas Ahrens
Prof. Donald V. Helmberger
Dr. Larry J. Burdick
Division of Geology & Planetary Sciences
California Institute of Technology
Pasadena, CA 91125 (3 copies)

Prof. Shelton Alexander
Prof. Charles A. Langston
Geosciences Department
403 Deike Building
The Pennsylvania State University
University Park, PA 16802 (2 copies)

Dr. Thomas C. Bache, Jr.
Dr. Thomas J. Sereno, Jr.
Dr. Jeffrey W. Given
Science Applications Int'l Corp.
10260 Campus Point Drive
San Diego, CA 92121 (3 copies)

Dr. Douglas R. Baumgardt, Dr. Zoltan A. Der
ENSCO, Inc.
5400 Port Royal Road
Springfield, VA 22151 (2 copies)

Dr. Eric P. Chael, Dr. Dale Breding
Dr. Larry S. Walker, Dr. Gary Mauth
Sandia National Laboratory
Division 9241
Albuquerque, NM 87185 (4 copies)

Dr. Theodore Cherry
Science Horizons, Inc.
710 Encinitas Blvd, Suite 200
Encinitas, CA 92024

Prof. Steven M. Day
Dept. of Geological Sciences
San Diego State University
San Diego, CA 92182

Dr. Mark D. Fisk
Mission Research Corporation
735 State Street
P.O. Drawer 719
Santa Barbara, CA 93102

Prof. Cliff Frolich, Dr. Lian-She Zhao
Institute of Geophysics
8701 North Mopac
Austin, TX 78759 (2 copies)

Ms. Lori Grant
Multimax, Inc.
311-C Forest Avenue, Suite 3
Pacific Grove, CA 93950

Prof. Henry L. Gray, Prof. Gary McCartor
Dept. of Physics
Southern Methodist University
Dallas, TX 75275 (2 copies)

Dr. Indra N. Gupta
Multimax, Inc.
1441 McCormick Drive
Landover, MD 20785

Dr. Richard A. Gustafson, Dr. Robert North
Dr. Jerry Carter
Center for Monitoring Research
1300 North 17th Street, Suite 1450
Arlington, VA 22209-2308 (4 copies)

Dr. Willard J. Hannon
Lawrence Livermore National Laboratory
P.O. Box 808
Livermore, CA 94550

Prof. David G. Harkrider
Boston College @ PL/GPE
29 Randolph Road
Hanscom AFB, MA 01731

Prof. Eugene T. Herrin, Jr.
Geophysical Laboratory
Southern Methodist University
Dallas, TX 75275

Prof. Robert B. Herrmann
Prof. Brian J. Mitchell
Dept. of Earth & Atmospheric Sciences
St. Louis University
St. Louis, MO 63156 (2 copies)

Prof. Bryan Isacks, Prof. Muawia Barazangi
Dept. of Geological Sciences
SNEE Hall
Cornell University
Ithaca, NY 14850 (2 copies)

Prof. Lane R. Johnson
Prof. Thomas V. McEvilly
Seismographic Station
University of California
Berkeley, CA 94720 (2 copies)

Prof. Thomas H. Jordan
Dept. of Earth, Atmospheric
and Planetary Sciences
Massachusetts Institute of Technology
Cambridge, MA 02139

Prof. Thorne Lay, Prof. Susan Schwartz
Institute of Tectonics
University of California, Santa Cruz
Santa Cruz, CA 95064 (2 copies)

Dr. Randolph Martin, III
New England Research , Inc.
76 Olcott Drive
White River Junction, VT 0500l

Dr. Keith L. McLaughlin
Dr. Jeffrey L. Stevens
Dr. Terrance G. Barker
Maxwell Laboratories, S-Cubed Division
P.O. Box 1620
La Jolla, CA 92038 (3 copies)

Mr. John R. Murphy, Dr. Theron J. Bennett
Maxwell Laboratories, S-Cubed Division
ll800 Sunrise Valley Drive, Suite 1212
Reston, VA 2209l (2 copies)

Dr. Dan N. Hagedorn, Dr. Ray Warner
Pacific Northwest Laboratories
Battelle Boulevard
Richland, WA 99352 (2 copies)

Prof. John A. Orcutt, Prof. Bernard Minster
Prof. Freeman Gilbert
IGPP, A-025
Scripps Institute of Oceanography
University of California, San Diego
La Jolla, CA 92093 (3 copies)

Dr. Jay J. Pulli
Radix Systems, Inc.
6 Taft Court
Rockville, MD 20850

Prof. Paul G. Richards, Prof. Lynn R. Sykes
Prof. William Menke, Prof. Arthur Lerner-Lam
Prof. David G. Simpson
Lamont-Doherty Earth Observatory
of Columbia University
Palisades, NY 10964 (6 copies)

Dr. Chandan K. Saikia, Dr. Bradley B. Woods
Woodward-Clyde Consultants
566 El Dorado Street
Pasadena, CA 91109-3245 (2 copies)

Prof. Charles G. Sammis, Prof. Keiichi Aki
Center for Earth Sciences
University of Southern California
University Park
Los Angeles, CA 90089 (2 copies)

Dr. Brian W. Stump, Dr. Steven R. Taylor
Dr. Wendee Brunish, Dr. Mark Hodgson
Dr. George Randall, Dr. Fredrick N. App
Los Almos National Laboratory
EES-3, MS C-335
Los Almos, NM 87545 (6 copies)

Prof. Clifford Thurber, Prof. Robert P. Meyer
University of Wisconsin-Madison
Dept. of Geology & Geophysics
1215 West Dayton Street
Madison, WS 53706 (2 copies)

Prof. M. Nafi Toksöz, Dr. William Rodi
Dr. Richard L. Gibson, Dr. Yingping Li
Earth Resources Laboratory
Mass. Institute of Technology
42 Carleton Street
Cambridge, MA 02l42 (4 copies)

Verification Program
Attn: Dr. Jay Zucca
Lawrence Livermore National Laboratory
P.O. Box 808, L205
Livermore, CA 94550 (12 copies)

Prof. Terry C. Wallace, Prof. Susan L. Beck
Dept. of Geosciences/SASO
University of Arizona
Tucson, AZ 85721 (2 copies)

U.S. GOVERNMENT AGENCIES

DARPA/OASB/Librarian
3701 N. Fairfax Drive
Arlington, VA 22303-1714

Dr. Ralph W. Alewine, III
Dr. Steven R. Bratt
Nuclear Treaty Programs Office
Rosslyn Gateway
1901 N. Moore Street, Suite 609
Arlington, VA 22209 (2 copies)

Dr. Robert R. Blandford
AFTAC/TT, Center for Monitoring Research
1300 N. 17th Street, Suite 1450
Arlington, VA 22209

Defense Technical Information Center
8725 John J. Kingman Road
Fort Belvoir, VA 22060-6218 (2 copies)

Dr. Anton W. Dainty, Dr. John J. Cipar
Dr. Katharine Kadinsky-Cade, Mr. Rong-Song Jih
Earth Sciences Division (PL/GPE)
Phillips Lab./ Geophysics Directorate
Hanscom AFB, MA 01731 (4 copies)

Dr. Stanley K. Dickinson
AFOSR/NM
110 Duncan Avenue, Suite B115
Bolling AFB
Washington, DC 20331-6448

Dr. Dale Glover
U.S. DIA/DT-IB
Washington, DC 20301

HQ AFTAC/CA
(STINFO)
1030 South Highway A1A
Patrick AFB, FL 32925-6001

HQ AFTAC/TTR
1030 South Highway A1A
Patrick AFB, FL 32925-6001 (12 copies)

HQ AFTAC/TTD
1030 South Highway A1A
Patrick AFB, FL 32925-6001 (3 copies)

Dr. Max Koontz, Dr. Joan B. Rohlfing
Dr. Leslie A. Casey, Dr. Stan Rudnick
U.S. Dept. of Energy/NN-20
Forrestal Building
1000 Independence Avenue
Washington, DC 20585 (4 copies)

Dr. Leonard E. Johnson
National Science Foundation
Division of Earth Sciences
4201 Wilson Boulevard, Suite 785
Arlington, VA 22230

Dr. William S. Leith
Mr. John Rodney Matzko
U.S. Geological Survey
920 National Center
Reston, VA 22092 (2 copies)

Mr. James F. Lewkowicz
Dr. Delaine T. Reiter, Mrs. Jeanne M. McPhetres
Earth Sciences Division (PL/GPE)
Phillips Lab/Geophysics Directorate
Hanscom AFB, MA 01731 (5 copies)

Dr. Don A. Linger, Dr. Michael Shore
U.S. DNA
6801 Telegraph Road
Alexandria, VA 22310 (2 copies)

Dr. Robert P. Massé
Denver Federal Center
Box 25046, Mail Stop 967
Denver, CO 80225

Office of the Secretary of Defense
DDR&E
Washington, DC 20330

Dr. Frank F. Pilotte
HQ AFTAC/TT
1030 South Highway A1A
Patrick AFB, FL 32925-6001

Phillips Laboratory / TL
5 Wright Street
Hanscom AFB, MA 01731

Phillips Laboratory
PL/SUL
3550 Aberdeen Avenue, SE
Kirtland AFB, NM 87117 (2 copies)

Phillips Laboratory
PL/XPG
Hanscom AFB, MA 01731

Dr. Robert E. Reinke
Field Command, DNA
FCDNA/FCTTS
1680 Texas Street, S.E.
Kirtland AFB, NM 87117-6008

Secretary of the Air Force
(SAFRD)
Washington, DC 20330

Dr. Owen J. Sheaks
Dr. William Roggenthen
Mr. Alfred Lieberman
Mr. Richard J. Morrow
Ms. Mona Dreicer
U.S. ACDA
320 21st Street NW
Washington, DC 20451 (5 copies)

Dr. Lawrence S. Turnbull, Jr.
Dr. John R. Filson
Katie Poley
Sean H. Doran
U.S. ACIS
Washington, DC 20505 (4 copies)

Center for Verification Research
Technical Library
P.O. Box 1148
8500 Cinder Bed Road
Newington, VA 22122-9998

OTHER RECIPIENTS

Dr. Don Albert
Lt. Col. Dick Jardine
U.S. ACRREL
72 Lyme Road
Hanover, NH 03755 (2 copies)

Dr. David M. Boore
Dr. Leif G. Wennerberg
Dr. Bernard A. Chouet
U.S. Geological Survey
345 Middlefield Road, MS 977
Menlo Park, CA 94025 (3 copies)

Dr. Arthur Frankel
U.S. Geological Survey
Denver Federal Center
Denver, CO 80225

Dr. Richard Lewis
Earthquake Engineering & Geophysics
U.S. Army Corps of Engineers
P.O. Box 631
Vicksburg, MS 39180

Dr. Ed McDonald
Naval Research Laboratory
4555 Overlook Avenue, SW
Washington, DC 20375

Mr. James Anderson, Mr. Rick Perez
Teledyne Brown Engineering
2111 Wilson Boulevard, Suite 900
Arlington, VA 22201-3058 (2 copies)

Prof. Charles B. Archambeau
Prof. Danny J. Harvey, Dr. Anatoli L. Levshin
University of Colorado, JSPC
Campus Box 583
Boulder, CO 80309 (3 copies)

Dr. Ralph J. Archuleta
Dept. of Geological Sciences
University of California at Santa Barbara
Santa Barbara, CA 93102

Dr. Jonathan Berger, Dr. Frank Vernon
Dr. Holly K. Given, Dr. Peter Davis
IGPP, A-025
Scripps Institute of Oceanography
University of California, San Diego
La Jolla, CA 92093 (4 copies)

Dr. G. A. Bollinger
Dept. of Geological Sciences
Virginia Polytechnic Institute
21044 Derring Hall
Blacksburg, VA 24061

Prof. Bruce A. Bolt
Prof. Barbara Romanowicz
Seismographic Station
475 McCone Hall
University of California
Berkeley, CA 94720 (2 copies)

Prof. Jon F. Claerbout
Dept. of Geophysics
Stanford University
Stanford, CA 94305

Prof. Robert W. Clayton
Seismological Laboratory
Division of Geological & Planetary Sciences
California Institute of Technology
Pasadena, CA 91125

Prof. Vernon F. Cormier
Dept. of Geology & Geophysics
University of Connecticut
Storrs, CT 06269-2045

Prof. Paul M. Davis, Prof. John Vidale
Dept. Earth & Space Sciences
University of California (UCLA)
Los Angeles, CA 90024 (2 copies)

Prof. Adam Dziewonski
Prof. Göran Ekström
Prof. James R. Rice
Hoffman Laboratory
Harvard Uninversity
20 Oxford Street
Cambridge, MA 02138 (3 copies)

Ronald W. Ewing
Ewing Associates
11535 Clara Barton Drive
Fairfax Station, VA 22039

Prof. John Ferguson
Prof. George McMechan
Center for Lithospheric Studies
University of Texas at Dallas
P.O. Box 688
Richardson, TX 75083-0688 (2 copies)

Prof. Stanley Flatté
Applied Sciences Building
University of California
Santa Cruz, CA 95064

Dr. Alexander Florence, Dr. Stephen Miller
SRI International
333 Ravenswood Avenue
Menlo Park, CA 94025-3493 (2 copies)

Dr. Bengt Fornberg
Exxon Engineering & Research Company
Clinton Township, Route 22 East
Annandale, NJ 08801

Prof. Donald Forsyth
Dept. of Geological Sciences
Brown University
Providence, RI 02912

Dr. Roger Fritzel
Pacific Sierra Research
1401 Wilson Blvd., Suite 1100
Arlington, VA 22209

Dr. Ivan Henson
Multimax, Inc.
1290 Highway A1A, Suite 206
Satellite Beach, FL 32937

Dr. Kevin Hutchenson
ENSCO, Inc.
445 Pineda Court
Melbourne, FL 32940

Prof. Alan Kafka, Prof. John Ebel
Dept. of Geology & Geophysics
Boston College
Chestnut Hill, MA 02167 (2 copies)

Dr. Cyrus P. Knowles
JAYCOR
1608 Spring Hill Road
Vienna, VA 22182

Prof. Leon Knopoff
University of California
Institute of Geophysics & Planetary Physics
Los Angeles, CA 90024

Dr. Richard LaCoss
MIT-Lincoln Laboratory
M-200B
P.O. Box 73
Lexington, MA 02173-0073

Prof. Fred K. Lamb
University of Illinois
Dept. of Physics
1110 West Green Street
Urbana, IL 61801

Dr. James Lawson
Oklahoma Geological Survey
P.O. Box 8
Leonard, OK 74043

Prof. Alan R. Levander
Dept. of Geology & Geophysics
Rice University, MS 126
Houston, TX 77005

Dr. Chris Lynnes
Hughes STX
7601 Ora Glen Dr., Suite 300
Greenbelt, MD 20770

Dr. J. Michael McKisic
Tracor Applied Sciences, Inc.
1601 Research Boulevard
Rockville, MD 20850

Dr. George Mellman
Sierra Geophysics
11255 Kirkland Way
Kirkland, WA 98033

Prof. James Ni, Prof. Thomas Hearn
Dept. of Physics
New Mexico State University
Las Cruces, NM 88003 (2 copies)

Prof. Jeffrey Park
Dr. Jonathan Lees
Dept. of Geology & Geophysics
Yale University
P.O. Box 208109
New Haven, CT 06520 (2 copies)

Prof. Robert Phinney
Geological & Geophysical Sciences
Princeton University
Princeton, NJ 08544-0636

Dr. Paul Pomeroy
Rondout Associates
P.O. Box 224
Stone Ridge, NY 12484

Mr. David Racine, Mr. Boomer Baumstark
Mr. Paul Kovacs
Teledyne Brown Engineer @ HQ AFTAC/TT
1030 South Highway A1A
Patrick AFB, FL 32925-6001

Dr. Richard Sailor
TASC, Inc.
55 Walkers Brook Drive
Reading, MA 01867

Prof. G. T. Schuster
Dept. of Geology & Geophysics
University of Utah
Salt Lake City, UT 84112

Prof. R. H. Shumway
Division of Statistics
University of California
Davis, CA 95616

Dr. Gregory E. van der Vink
IRIS, Inc.
1616 North Fort Myer Drive, Suite 1050
Arlington, VA 22209 (2 copies)

Prof. Stewart W. Smith
Prof. Stephen D. Malone
Geophysics AK-50
University of Washington
Seattle, WA 98195 (2 copies)

Prof. Jeremiah Sullivan
University of Illinois at Urbana-Champaign
Dept. of Physics
1110 West Green Street
Urbana, IL 61801

Prof. Pradeep Talwani
Dept. of Geological Sciences
University of South Carolina
Columbia, SC 29208

Prof. Leo T. Teng
University of Southern California
University Park
Los Angeles, CA 90089

Dr. Karl F. Veith
EG&G
2341 Jefferson Davis Highway, Suite 801
Arlington, VA 22202

Dr. William Wortman
Mission Research Corporation
8560 Cinderbed Road, Suite 700
Newington, VA 22122

Prof. Francis T. Wu
Dept. of Geological Sciences
State University of New York, Binghamton
Vestal, NY 13901

FOREIGN RECIPIENTS

Dr. V. V. Adushkin
Dr. I. O. Kitov
Inst. for Dynamics of Geospheres
Russian Academy of Science
Moscow, Russia (2 copies)

Dr. Peter Basham
Earth Physics Branch
Geological Survey of Canada
1 Observatory Crescent
Ottawa, Ontario,CANADA K1A OY3

Prof. Ari Ben-Menahem
Dept. of Applied Mathematics
Weizman Institute of Science
Rehovot, ISRAEL 951729

Dr. Michel Bouchon
I.R.I.G.M.-B.P. 68
38402 St. Martin D'Heres
Cedex, FRANCE

Dr. Michel Campillo
Observatorie de Grenoble
I.R.I.G.M.-B.P. 53
38041 Grenoble, FRANCE

Dr. Lawrence A. Drake
Observatorio San Calixto
Casilla 12656, La Paz, BOLIVIA

European-Mediterranean Seismological Centre
CSEM
c/o LPG
BP 12, 91680 Bruyeres-le-Chatel
FRANCE

Dr. Peter Firbas
Institute of Physics of the Earth
Masaryk University Brno
Jecna 29a
612 46 Brno, CZECH REPUBLIC

Prof. Hans-Peter Harjes
Institute for Geophysik
Ruhr University/Bochum
P.O. Box 102148
463 Bochum 1, GERMANY

Dr. Manfred Henger
Fed. Inst. for Geosci. & Nat'l Res.
Postfach 510153
D-3000 Hanover 51, GERMANY

Dr. Eystein Husebye
Inst. for Solid Earth Physics
University of Bergen
Allegation 40
N-5007 Bergen, NORWAY

David Jepsen
Nuclear Monitoring Section
Geology & Geophysics
Bureau of Mineral Resources
G.P.O. Box 378
Canberra, AUSTRALIA

Ms. Eva Jöhannisson
Senior Research Officer
National Defense Research Institute
P.O. Box 27322
S-102 54 Stockholm, SWEDEN

Prof. Brian L.N. Kennett
Research School of Earth Sciences
Institute of Advanced Studies
G.P.O. Box 4
Canberra 2601, AUSTRALIA

Dr. Peter Marshall
Dr. Alan Douglas
Ministry of Defense/Procurement Executive
Blacknest, Brimpton
Reading FG7-4RS
ENGLAND (2 copies)

Dr. Bernard Massinon
Dr. Pierre Mecheler
Societe Radiomana
27 rue Claude Bernard
75005 Paris, FRANCE (2 copies)

Prof. Keith Priestley
Dept. of Earth Sciences
Madingley Rise, Madingley Road
University of Cambridge
Cambridge CB3 0EZ, ENGLAND

Dr. Frode Ringdal
Dr. Svein Mykkeltveit
NTNF/NORSAR
P.O. Box 5l
N-2007 Kjeller, NORWAY (2 copies)

Dr. Jorg Schlittenhardt
Federal Inst. for Geosciences &
Natural Resources
Stilleweg 2, D-3000 Hannover 51
GERMANY

Dr. A. Shapira
Seismology Division
Inst. for Petroleum Research & Geophysics
Holon, ISRAEL

Dr. C. Srinivasan
Seismology Section
National Inst. of Rock Mechanics
New Deli, INDIA

Dr. Tuncay Taymaz
Istanbul Technical University
Dept. of Geophysical Engineering
Maslak-80626, Istanbul, TURKEY